Applied Catalysis B: Environmental 221 (2018) 490–509

Contents lists available at ScienceDirect

Applied Catalysis B: Environmental

journal homepage: www.elsevier.com/locate/apcatb

Evolution of the structure of unpromoted and potassium-promoted ceria-supported nickel catalysts in the steam reforming of ethanol

Grzegorz Słowik*, Magdalena Greluk, Marek Rotko, Andrzej Machocki

University of Maria Curie-Skłodowska, Faculty of Chemistry, Department of Chemical Technology, Lublin, Poland

ARTICLE INFO

Keywords:
Steam reforming of ethanol
Stability of nickel catalysts
Nickel crystallites size
Potassium promoter
Electron microscopy

ABSTRACT

Unpromoted and potassium-promoted Ni/CeO_2 catalysts, fresh, reduced and used in the SRE were characterized by TEM (as a leading method), SEM, XRD, hydrogen chemisorption, H_2-TPR and Raman spectroscopy. The evolution of the nature and the size of the nickel active phase (different in both catalysts) as well as distribution of potassium is disclosed. The promoter does not protect the catalyst against formation of carbonaceous deposit and does not improve its stability in the SRE. More important is high dispersion of nickel. Smaller nickel crystallites in Ni/CeO_2 ensure its better stability. In both catalysts, fragments of nickel (devoid of potassium in the case of KNi/CeO_2) are pushed from ceria by carbonaceous fibres formed. Their nature is different in both catalysts. On the Ni/CeO_2 amorphous (disordered) long and thick as well as short and thin graphitic fibres are formed. The KNi/CeO_2 produces very large amount of only graphitic fibres, longer and thicker than those in unpromoted catalyst. Much intensive production of graphitic fibres, which with time-of-stream can encapsulate greater number of nickel crystallites, is considered as responsible for faster deactivation of KNi/CeO_2 catalyst in the SRE.

1. Introduction

Hydrogen is considered as a high-energy and alternative energy source, which can play an important role in reducing emission to the environment. One of the most efficient methods of the production of hydrogen is the steam reforming of ethanol (SRE). If the process runs in the most desirable way, it is possible obtaining 6 mol of hydrogen from 1 mol of ethanol (according to the reaction $C_2H_5OH + 3H_2O \rightarrow 6H_2 + 2CO_2$) [1–3]. Otherwise, the decrease in the efficiency of hydrogen production takes place by production of undesirable products such as acetaldehyde, acetone, methane and ethylene. These side products can also lead to carbon formation and catalyst deactivation [3–6]. For these reasons, in the steam reforming of ethanol, suitably selected catalyst plays an important role in achieving selective and complete ethanol conversion, as well as it is essential for the process to be economically profitable [2,3,6]. Active catalysts should maximize hydrogen selectivity, inhibit coke formation and by-products production [7]. Therefore, a high efficiency in conversion of ethanol, a high selectivity to hydrogen and, at the same time, a high resistance to deactivation under the SRE process conditions are important factors in designing the catalyst for the steam reforming of ethanol. The most commonly used metallic active phases in the catalytic steam reforming of ethanol are very active and efficient noble metals and, as a significantly less expensive alternative, transition metals, such as nickel or cobalt [2].

Reports are very often presented on catalysts with the nickel active phase [5,8,9,10]. The nickel-based catalysts were reported to be more active in the steam reforming of ethanol, they have better properties in the cleavage of C—C bonds [11,12] but they have a higher selectivity to carbon monoxide and methane formation than cobalt-based catalysts [13]. However, the use of nickel as the active phase in the catalytic system has also some other drawbacks, which include escalated production of the carbon deposit which leads to falling-off activity and selectivity of the catalyst in the SRE process [6]. In order to reduce these negative effects various improvements were proposed. One of them is synthesis of very small nickel crystallites, and then their stabilization by using an oxide support material with redox properties, such as CeO_2, which would also affect the catalytic properties by a strong interaction with the active metal [14]. An another improvement is addition of the promoter with alkaline properties which would have a positive impact on the stability and reactivity of such catalytic system. The addition of the alkali promoter (e.g. potassium) can improve catalytic properties of the nickel-based system; the electron enrichment of nickel by the presence of alkali can also modify interaction between

* Corresponding author at: University of Maria Curie-Skłodowska, Faculty of Chemistry, Department of Chemical Technology, 3 Maria Curie-Skłodowska Square, 20-031 Lublin, Poland.
E-mail address: Grzegorz.Slowik@poczta.umcs.lublin.pl (G. Słowik).

http://dx.doi.org/10.1016/j.apcatb.2017.09.052
Received 31 May 2017; Received in revised form 31 August 2017; Accepted 22 September 2017
Available online 23 September 2017
0926-3373/

adsorbed intermediate reaction products and the metallic active phase [15]. Frusteri et al. [15] showed that addition of the alkali metal (Li, Na, K) to the nickel catalyst increases its ability to prevent carbon formation and increases the catalyst activity and stability in the SRE process [15]. Another method for elimination or reduction of the carbon deposit formation is mentioned above suitable choice of the catalyst support. In the recent years many studies showed a high resistance of ceria to formation of carbonaceous deposits [16–20]. It was suggested that the catalyst with the CeO_2 support has a high oxygen storage capacity and mobility what enables a more efficient gasification of carbon atoms adsorbed on the surface of the catalyst.

Beside of selection of the appropriate support and application of the alkaline promoter, catalytic properties of catalysts depend also on their features, such as their structure, morphology and crystallites size of the active phase. The dispersion as well as the average crystallites size of the active metal belong to the most decisive parameters characterizing supported catalysts [21,22], which are important for the activity, selectivity and stability of the catalyst in the catalytic processes. The catalytic activity of the heterogeneous catalysts depends on the dispersion of the metallic active phase and its active surface area [21–23], and it usually increases with increasing dispersion of the active metal and decreasing of its crystallites size [21,23]. Moreover, the crystallites shape and the size distribution are closely related to the mechanism of a catalytic reaction, which dependents on exposed crystal planes available for reactants [21,24]. The share of various individual active sites on the active phase is closely related to its crystallites size [25–27].

For determination of the crystallites size of metallic active phase usually X-ray diffraction (XRD), hydrogen chemisorption and transmission electron microscopy (TEM) are used [21,22,28], but sometimes for the same catalyst different results are founded from different methods. The differences in measurements of the crystallites size usually results from method limitations. In the case of XRD measurements such limitation may be the fact that this method does not measure very small crystallites. The measurement limitations can also concern hydrogen chemisorption which can be diminished by strong interactions between metal and its support [21,29]. Furthermore, our previous work [21] and others papers [30–32] showed that the temperature of hydrogen chemisorption measurements can significantly influence obtained value of the mean size of metal crystallites. Despite the fact that the hydrogen chemisorption is a simple, common and cheap method, it requires a suitable temperature of measuring. In order to obtain objective measurements of the average size of metal crystallites on the basis of hydrogen chemisorption it is important to find a correlation between this method and other methods allowing precisely estimating the crystallites size of the active phase. In this case, the most objective and reliable method of measuring the crystallite size becomes the transmission electron microscopy which gives a direct view of the crystallites size and shape, their dispersion, and simultaneously allows to observe the structure and morphology of the catalyst and relations between the active phase, the support and the promoter [29].

This work shows studies of the structure and morphology changes of unpromoted and potassium-promoted nickel catalysts with the ceria support during their three-stage functioning (fresh, reduced and used in the SRE). The key role in these studies plays the high resolution electron microscopy which allowed us to directly observe all changes in the structure and morphology of both catalysts in those individual stages. The HRTEM with FFT and the STEM-EDS characteristics allow us to identify phases, to determine crystallites size and dispersion of the active phase as well as distribution of elements in the catalysts. The scanning electron microscopy enabled characterization of the nature of carbonaceous deposits formed in the SRE. These studies were supplemented with XRD, hydrogen chemisorption, TPR studies, Raman spectroscopy and catalytic tests, which together with electron microscopic studies give a full view on to structural-performance relationships and on changes taking place within the both catalytic systems during their operation stage. As the dispersion of the nickel active phase plays an important role in behaviour of the catalysts in the SRE it was determined by three independent methods. The measurements of the average nickel crystallites size performed by XRD and TEM were compared with those from data of the total and strong hydrogen chemisorption. On the basis of these results the most suitable chemisorption temperatures for unpromoted and promoted with potassium nickel catalysts were indicated, which allow determining the proper crystallites size of the nickel active phase, compatible with the crystallites size determined by the most direct and objective method which is the transmission electron microscopy. The paper presents also the influence of addition of the potassium promoter to the nickel catalyst as well as the influence of the crystallites size of the nickel active phase on the catalytic activity, selectivity and resistance to production of various kinds of carbon deposits during the ethanol conversion process.

2. Materials and methods

2.1. Catalyst preparation

The Ni/CeO_2 and KNi/CeO_2 catalysts were prepared by impregnation of the cerium oxide support. Prior to impregnation, the ceria support (Aldrich) was dried at 110 °C for 3 h. For the Ni/CeO_2 catalyst, an aqueous solution of nickel nitrate with citric acid CA (Ni/CA = 1/1 mol/mol) was used for impregnation. In the case of preparation of the potassium promoted KNi/CeO_2 catalyst, an aqueous solution of potassium nitrate was applied for the second impregnation of the Ni/CeO_2 catalyst. After each impregnation, the catalyst precursors were dried at 110 °C for 12 h, then calcined at 420 °C with the heating rate of 2.2 °C/min up to the calcination set point and maintained for 1 h at this temperature. Before all measurements the catalysts were reduced with hydrogen at 420 °C for 1 h. The in situ XRD, the HRTEM with FFT and the electron diffraction measurements confirmed complete reduction of nickel oxide to metallic nickel at these conditions. The total surface area of the reduced Ni/CeO_2 catalyst was equal to 56.3 m^2/g and the active (nickel) surface area was 22.6 m^2/g while in the case of the KNi/CeO_2 catalyst − they were equal to 31.6 m^2/g and 7.9 m^2/g, respectively.

2.2. Steam reforming of ethanol studies

The reaction of ethanol conversion (SRE) was carried out at 420 °C under atmospheric pressure, in a fixed bed continuous-flow quartz reactor, using 0.1 g (0.15-0.30 mm) of the catalyst diluted (1/10 w/w) with 0.15-0.30 mm grains of quartz. The flow rate of the reaction mixture vapours was 100 ml/min. The reaction mixture was composed of ethanol and water vapours with the 1/12 ($EtOH/H_2O$) mol/mol ratio. This $EtOH/H_2O$ ratio is low enough to clearly show all changes in the morphology of the catalyst under SRE conditions. The products of the reaction were analyzed with two on-line gas chromatographs. The first of them, Bruker 450-GC, equipped with three columns: CP-Molsieve 5A, Molsieve 5A, Porapak Q and a TCD detector was used for analysis of carbon-containing products. The carrier gas in this system was helium. The second of the chromatographs, Bruker 430-GC, was used for analysis of hydrogen. This system was equipped with Molsieve 5A column and a TCD detector. In this case the carrier gas was argon.

The total conversion of ethanol X_{EtOH}, conversion of water X_{H2O} and conversion of ethanol into particular carbon-containing products, X_{CP}, were calculated on the basis of their concentrations before and after the reaction, with a correction introduced for the change in the gas volume during the reaction, from Eq. (1):

$$X_{EtOH} = \frac{C_{EtOH}^{in} - C_{EtOH}^{out} K}{C_{EtOH}^{in}} \cdot 100\%;\ X_{H2O} = \frac{C_{H2O}^{in} - C_{H2O}^{out} K}{C_{H2O}^{in}} \cdot 100\%;\ X_{CP} = \frac{C_{CP}^{out} K}{(n/2) C_{EtOH}^{in}} \cdot 100\% \quad (1)$$

where C_{EtOH}^{in} and C_{H2O}^{in} represent molar concentrations of ethanol and

water in the reaction mixture, mol%; C_{EtOH}^{out} and C_{H2O}^{out} are molar concentrations of ethanol and water in the post-reaction mixture, mol%; C_{CP}^{out} is the molar concentration of carbon-containing products in the post-reaction mixture, mol%; n is the number of carbon atoms in the carbon-containing molecule of the reaction product; K is the volume contraction factor ($K = C_c^{in}/C_c^{out}$ where: $C_c^{in}$and C_c^{out} are molar concentrations of carbon in ethanol + water fed to the reaction and in all carbon-containing compounds which were present in post-reaction gases, respectively).

The selectivity of ethanol conversion into individual carbon-containing products was expressed as $(X_{CP}/X_{EtOH}) \cdot 100$. The carbon mass balance, based on the carbon selectivities, was close to 100 ± 3%. The selectivity of hydrogen formation was determined from the Eq. (2):

$$H_2 - \text{selectivity} = \frac{C_{H2}^{out}}{C_{H2}^{in} + 2C_{CH4}^{out} + 2C_{CH3CHO}^{out}} \cdot 100\% \quad (2)$$

where C_{out} refers to the molar concentrations of the hydrogen-containing reaction products found in the post-reaction gases, mol%.

2.3. Low-temperature adsorption of nitrogen

The Brunauer-Emmett-Teller (BET) surface area of the catalysts was determined by low-temperature (−196 °C) nitrogen adsorption in the static-volumetric ASAP 2425 analyser (Micromeritics).

2.4. Hydrogen chemisorption measurements

Hydrogen chemisorption isotherms were measured in a standard, commercial volumetric apparatus (Micromeritics, ASAP 2020C). The reactor was loaded with 0.9 g of the catalyst. Prior to the measurements, the catalysts were in-situ reduced in flowing hydrogen with the temperature programmed from ambient to 420 °C with the heating rate of 10 °C/min. The 420 °C temperature was maintained for 1 h. After reduction, the samples were evacuated for 2 h at the reduction temperature. Then, under the vacuum of 3.8×10^{-7} Pa, the catalyst samples were cooled down to the temperature of chemisorption. Hydrogen chemisorption isotherms were measured in the range of 40–160 or 180 °C and in the pressure range of 15–475 mmHg. Subsequently, the sample of the catalyst was evacuated for 30 min, keeping the constant temperature (the same at which the first isotherm was taken), and the second isotherm of weak chemisorption was recorded. The strong chemisorption isotherm of hydrogen was calculated as a difference between the first (total) and the second (weak) isotherms. The uptake of hydrogen (total, weak and strongly chemisorbed) was determined by extrapolating the straight-line portions of isotherms to the zero pressure. For measurements of the chemisorption isotherms at various temperatures always the new catalyst sample was used. The average size of nickel crystallites was calculated from the equation $d = (6 \times 10^3)/(g_{Ni} \times S_{Ni})$, where g_{Ni} is the density of nickel and S_{Ni} is the surface area of nickel (m^2/g_{Ni}), assuming that nickel crystallites are spherical and one hydrogen atom is adsorbed on an area occupied by one surface metal atom and the surface area occupied by one atom of hydrogen equals to 0.065 nm^2.

2.5. TEM measurements

The unpromoted and potassium promoted nickel catalysts in the fresh form were grinded in an agate mortar to fine powders. The resulting powder of each catalyst was poured with 99.8% ethanol (POCH) to form slurry which subsequently was inserted into an ultrasonic homogenizer for 20 s. Then, the catalyst-containing slurry was pipetted and supported on a 200 mesh copper grid covered with lacey formvar and stabilized with carbon (Ted Pella Company) and left on a filter paper for ethanol evaporation. The samples deposited on the grid were inserted to a single-tilt holder and moved to the electron microscope.

The reduced catalysts (in a fixed-bed reactor with hydrogen flow rate of 100 ml/min at 420 °C) and the catalysts used in the SRE were transferred in a closed reactor to a glovebox. The reactor was opened and the catalyst was prepared for TEM measurements in the glovebox filled with argon (it protected the catalyst from oxidation). The catalysts were deposited on the copper grid covered with lacey formvar and stabilized with carbon. Next, the each catalyst deposited on the grid was inserted into the vacuum transfer holder (Gatan); the holder was closed and the catalyst was transferred in argon atmosphere to the microscope.

The high-resolution electron microscope Titan G2 60–300 kV (FEI Company), equipped with: the field emission gun (FEG), monochromator, three condenser lenses system, the objective lens system, image correction (C_s-corrector), HAADF detector and EDS (Energy Dispersive X-Ray Spectroscopy) spectrometer was used to studies of the catalysts. Microscopic studies of the catalysts were carried out at an accelerating voltage of the electron beam equal to 300 kV.

The size and the shape of particles in the fresh, reduced and used in the SRE Ni/CeO_2 and KNi/CeO_2 catalysts were determined by using the high resolution TEM (HRTEM) imaging with FFT or STEM-EDS analysis. Phase separation (crystal lattice of the cerium oxide and crystal lattice of the nickel active phase) was performed with the FFT by using a masking available in the Gatan Digital Micrograph software package. On the basis of the FFT generated from HRTEM images individual phases with various crystallographic orientations derived from the ceria support, the active phase in various forms, NiO (oxide) and Ni^0 (reduced) as well as amorphous and graphite carbon (in used catalysts) were identified. Then, the mask was imposed on the FFT in order to separate crystallites of the active phase (NiO or Ni^0) from crystallites of the support or carbon deposits present in the HRTEM images. The measurements of crystallites size of the separated active phase allowed us to determine distribution of crystallites size. The particles size distribution was obtained by measuring diameter of about 150 particles. The average size of particles was calculated from the Eq. (3):

$$d_{average} = \sum N_i D_i / \sum N_i \quad (3)$$

where: N_i – the number of metal crystallites in a specific size range, D_i – the average diameter in each diameter range.

The elements mapping was carried out in the STEM mode by collecting point by point EDS spectrum of each of the corresponding pixels in the map. The collected maps were presented in the form of a matrix of coloured pixels with the intensity corresponding to the amount of the element.

2.6. SEM measurements

The catalysts samples after 24 h and 100 h in the SRE were applied to aluminum tables covered by carbon conductive tabs and were transferred to the electron microscope. The Quanta 3D FEG scanning electron microscope (SEM) of the FEI Company, equipped with ETD detector (*Everhart-Thornley Detector*) was used for imagining the catalysts samples. Microscopic studies of catalysts were carried out at an accelerating voltage 20/30 kV.

Qualitative and quantitative contents of main elements in the fresh catalysts were determined from EDS spectra collected by using the FEI Quanta 3D FEG scanning electron microscope, equipped with the EDS spectrometer.

2.7. XRD measurements

Before XRD measurements, the catalysts were in-situ reduced at 420 °C in hydrogen with a flow rate of 100 ml/min in the XRK 900 reactor chamber (Anton Paar). X-ray diffraction patterns were collected at two temperatures, at 30 °C for the fresh (oxide) samples and at 420 °C for reduced samples, by means of the Empyrean (PANalytical) X-ray

diffractometer, using CuKα radiation ($\lambda = 1.54 \times 10^{-10}$ m). The analyses were recorded in the 2θ range between 10° and 110°. For measurements at 30 °C the average crystallites size of nickel oxide was calculated from the Scherrer equation [29] using the NiO (111) peak located at 2θ = 37.3° and the peak of NiO (200) located at 2θ = 43.3°. The metallic nickel particles size in reduced catalysts was calculated also from the Scherrer formula using the Ni (111) peak located at 2θ = 44.6°. A standard crystal of cerium oxide was used as a reference material for determination the instrumental line broadening.

2.8. TPR measurements

The H_2-TPR measurements were carried out in the AutoChem II 2920 (Micromeritics) apparatus equipped with a quartz tube flow reactor and the thermal conductivity detector (TCD). 50 mg of the catalyst with a grain size of 0.3-0.6 mm was placed in the reactor. Prior to the H_2-TPR, the samples were pre-treated under a 5% O_2 in He mixture. The reducing gas was a mixture of 5% H_2 in Ar flowing through the reactor at a rate of 30 cm^3/min. The heating rate was 10 °C/min. The Gaussian + Lorentzian function available at the PeakFit SeaSolve software was used for fitting peaks.

2.9. Raman spectroscopy measurements

The Raman spectroscopy was applied to identify the nature of carbonaceous deposits present in the used catalysts. The spectra were recorded in the Raman microscope (inVia Reflex, Renishaw) with Raman dispersive system, using the red 785 nm semiconducting laser. In order to avoid sample overheating, 0.5 mW of the laser power was used. The spectra were recorded in the range of 100–3200 cm^{-1} in order to allow reliable fitting. The Lorentzian function (available at the PeakFit SeaSolve software) was used for fitting and all the fit parameters such as line positions, amplitudes, widths and areas were allowed to vary.

3. Results and discussion

3.1. TEM characterization of fresh and reduced catalysts

Both catalysts contain about 10 wt.% of nickel while promoted catalyst contains also about 2 wt.% of potassium (Fig. S1 and Table S1).

The electron diffraction of the fresh and reduced, unpromoted and potassium promoted catalysts (Fig. S2 and S3) showed very intense rings and peaks (with the characteristic values described in Table S2) coming from the ceria support. Low-intense rings and peaks were observed for NiO with crystallographic orientation (111), (200) and (220). In the reduced catalyst low-intense rings and peaks were observed for metallic nickel with the crystallographic orientations (111) and (200). The addition of the potassium promoter to the nickel catalyst does not have any influence on its crystallographic structure. It suggests that potassium promoter does not form any crystalline structures with nickel or with the ceria support in both forms (oxide and reduced) of the catalyst. Ogo et al. [33] showed that the addition of the potassium promoter to the catalyst caused surrounding of the active phase by an amorphous potassium oxide – the potassium promoter created with oxygen an amorphous form and therefore, it was not possible to observe any crystalline structure of potassium with others metals.

The STEM-EDS analysis of the fresh unpromoted Ni/CeO_2 catalyst (Fig. 1) shows a good dispersion of nickel particles on the ceria support. It proves that preparation method led to a good dispersion of small clusters (crystallites) of nickel on the ceria support.

Also the STEM-EDS analysis of the fresh potassium-promoted KNi/CeO_2 catalyst (Fig. 2) show a good dispersion of small nickel oxide crystallites on the ceria support and a very good dispersion of potassium promoter in the whole catalyst. At some areas on the Ni map it is observed that nickel crystallites are also located very close to each other, what can be observed in the Ni map as suggested one large crystallite. Nevertheless, the preparation method applied in this work led to the high dispersion and small crystallites of the nickel active phase.

Fig. 3 presents crystal phases in the fresh Ni/CeO_2 catalyst identified by the high resolution electron microscopy and FFT. In this catalytic system the nickel active phase was observed as nickel oxide with crystallographic orientations (111) and (200). Phase identification allowed also defining number of cerium oxide crystallites with various crystallographic orientations of planes: (111), (200), (220), (311), (222) and (400). The use of masking method allowed us to separate NiO (111) and Ni(200) crystallite planes from crystallites of the ceria support. Fig. 3 presents also phases separation in the fresh Ni/CeO_2 catalyst. With the purple colour NiO(111) crystallites are marked, green colour indicates NiO(200) crystallites and the turquoise colour marks crystallites of CeO_2.

The separation of NiO crystallites from the support allowed us to measure precisely the size of these crystallites (Fig. 4) and to determine their distribution in the catalyst. The NiO crystallites size distribution is also shown in Fig. 4; the average size of NiO crystallites in the fresh Ni/CeO_2 catalyst is 4.90 nm.

The HRTEM image in Fig. 5A shows the nickel active phase (in the oxide form) as NiO (200), located on the ceria support with crystallographic orientation (111). The given parameters and the crystallographic structure observed in Fig. 5A for nickel oxide correspond very well to the Fm3 m space group and the cubic crystal lattice (Fig. 5B).

The phase identification of the fresh KNi/CeO_2 catalyst by using the high resolution electron microscopy and FFT is presented in Fig. 6. The nickel active phase in the catalyst is identified as NiO with similar crystallographic planes as in the case unpromoted nickel catalyst. Also the phases originating from the ceria support contain similar crystallographic orientations ((111), (200), (220), (311) and (222)). The separation of NiO crystallites from ceria support crystallites enables better distinguishing of these two phases. Red and yellow colours indicate NiO crystallites dispersed on the ceria support (turquoise colour). The NiO crystallites size distribution is also shown in Fig. 6. The average NiO crystallites size in the fresh KNi/CeO_2 catalyst is 5.11 nm, i.e. it is larger a little than that in the case of the unpromoted catalyst (Fig. 4).

Fig. 7 shows an image of a fragment of the fresh KNi/CeO_2 catalyst obtained by the high resolution transmission electron microscopy. In the fresh, oxide form of the KNi/CeO_2 catalyst the active phase was observed as NiO crystallites with various crystallographic orientations (111), (200) and (220). The specified parameters and crystallographic structure of NiO crystallites seen in Fig. 7 correspond to the same Fm3 m space group and the cubic crystal lattice as in the unpromoted catalyst. Nickel oxide crystallites of the active phase are located on the ceria support with crystallographic orientation (111).

Fig. 8 shows STEM-EDS analysis of the reduced Ni/CeO_2 catalyst. The Ni + Ce EDS map presents good dispersion of nickel on the ceria support. The nickel active phase forms small crystallites on the ceria support. Some of these crystallites are located very close to others, what can be observed in the Ni map as suggested larger crystallite. However, these crystallites remain separated and only create the group of crystallites.

EDS maps (presented in Fig. 9) of the reduced KNi/CeO_2 show also (as in the case Ni/CeO_2 catalyst) a good dispersion of metallic nickel on the ceria support and a very good dispersion of potassium in the catalyst. The reduction has not changed distribution of potassium on the catalyst surface. However, nickel crystallites observed in the reduced KNi/CeO_2 catalyst are larger than those observed in the Ni/CeO_2 catalyst. The addition of potassium to the nickel catalyst caused increasing of the crystallites size of the metallic nickel. It proves that the addition of potassium to the nickel catalyst favours sintering of nickel crystallites. The similar phenomenon was also observed in the case of the cobalt active phase supported on cerium oxide [21].

The phase identification and separation, the nickel crystallites shape and size as well as their distribution in the unpromoted Ni/CeO_2

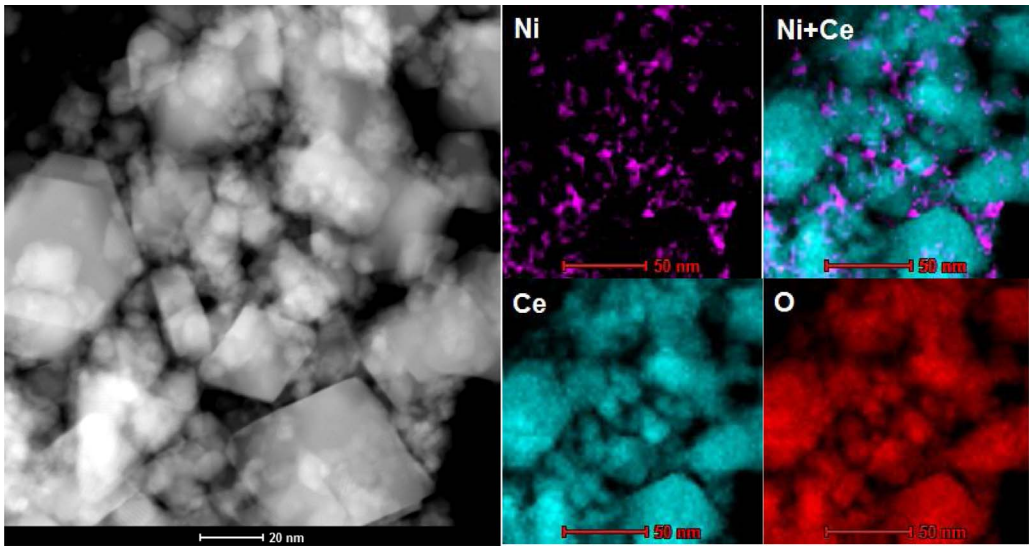

Fig. 1. STEM-EDS analysis of fresh Ni/CeO_2 catalyst.

catalyst are presented in Fig. 10. Based on FFT generated from the HRTEM image of the Ni/CeO_2 catalyst, the Ni (111) phase was identified for metallic nickel. The phase separation allows better distinguishing of nickel crystallites from the ceria support. The precise measurements of the crystallites size were carried out and they allowed us to determine accurately distribution and the average crystallites size of the nickel active phase to be 3.50 nm. The average size of nickel crystallites is smaller than that of initial nickel oxide (Fig. 4). However, new larger crystallites of metallic nickel also appeared.

The high resolution transmission electron microscopy analysis of the reduced Ni/CeO_2 catalyst from the other area (Fig. 11) allows finding also the Ni (200) face beside the Ni (111) face. The characteristic interplanar distances and the crystallographic structure observed in Fig. 11 for metallic nickel correspond very well to the Fm3 m space group and the cubic crystal lattice. For the ceria support crystallites, there were observed following crystallographic planes orientations: (111), (200), (220), (311), (222), (331).

Fig. 12 presents HRTEM images of a fragment of the reduced KNi/CeO_2 catalyst as well as phase identification and the nickel crystallites size distribution. Among identified phases, nickel crystallites were observed in the metallic form with crystallographic orientation (111). For the ceria support, phases with crystallographic orientations (111) and (220) were found. The interplanar distances and the crystallographic structure observed in Fig. 12 for metallic nickel fulfill very well to the

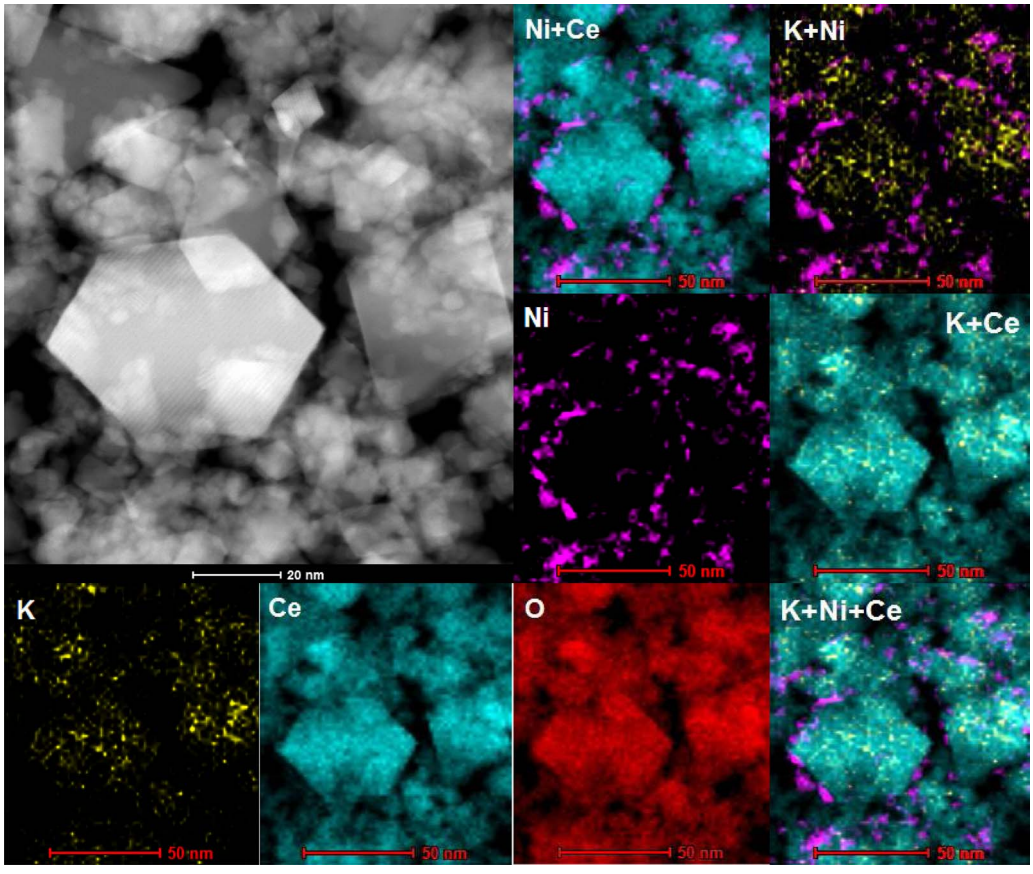

Fig. 2. STEM-EDS analysis of fresh KNi/CeO_2 catalyst.

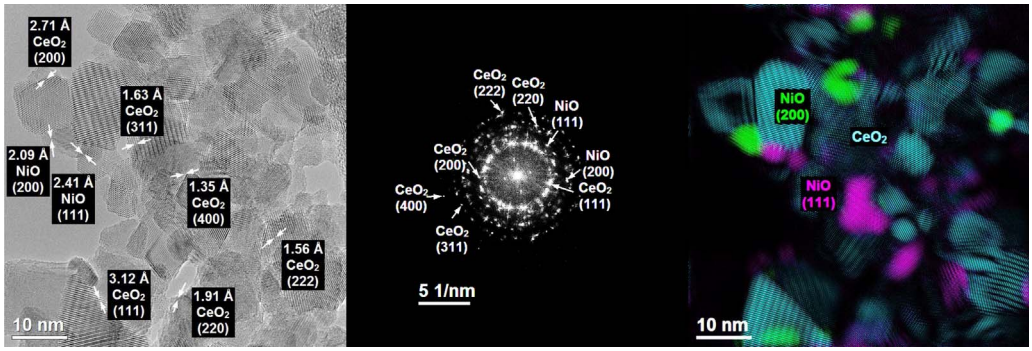

Fig. 3. HRTEM image and FFT with phase identification in the fresh Ni/CeO_2 catalyst.

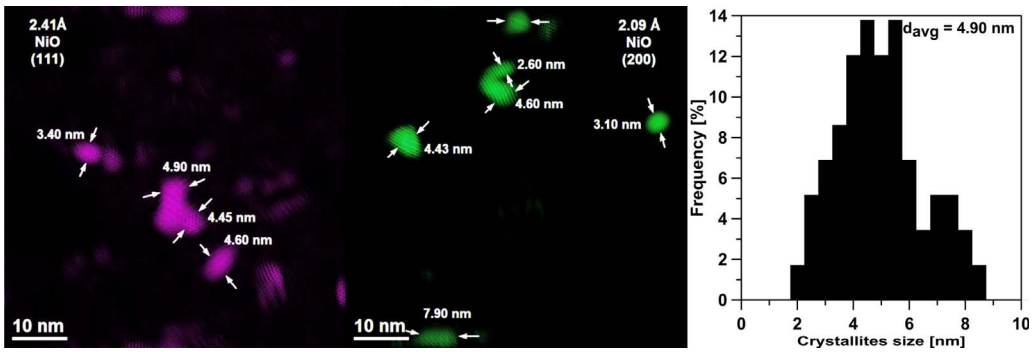

Fig. 4. Examples of NiO crystallites size measurements and their distribution in the fresh Ni/CeO_2 catalyst.

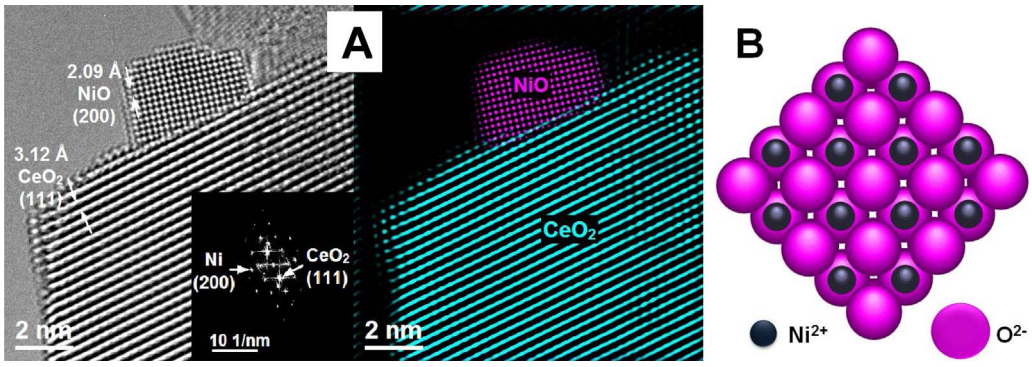

Fig. 5. (A) HRTEM image and FFT with phase identification of the fresh Ni/CeO_2 catalyst; (B) computer simulation of the NiO crystallographic structure.

same Fm3 m space group and cubic crystal lattice as found in the unpromoted catalyst. In Fig. 12 purple color indicates nickel crystallites dispersed on the ceria support marked with the turquoise color. The average size of nickel crystallites measured after their separation from the support is 8.43 nm.

The increase of the average size of crystallites after reduction at 420 °C, from 5.11 nm for the NiO form to 8.43 nm for the metallic (Ni^0) form, was observed only in the case of the potassium-promoted catalyst (Table 1). Based on these results it can be stated that the addition of the potassium promoter to the Ni-based catalyst favours sintering of nickel crystallites. Inversely, the reduction of the unpromoted catalyst caused decreasing of the size of the nickel active phase crystallites from 4.90 nm for the oxide form to 3.50 nm for the reduced (metallic) nickel form. The calculated ratio of the average crystallites size of the nickel active phase in the reduced form (Ni^0) to that of the oxidized form (NiO) is equal 0.71 for unpromoted and 1.65 for potassium-promoted catalysts.

Among many parameters that are associated with the catalyst performance it is known that the particle size of the active phase plays a key role and it is inseparably connected with the important features of the catalyst such as resistance to the formation of carbonaceous deposit or resistance of the active phase to oxidation. The metal crystallites size is an important factor in the tendency of the metal to oxidation under the reaction conditions. The optimum particles size of metal depends on its nature, the type and the nature of the support and on conditions of the catalytic process [34]. The surface of the catalyst can be easily varied and adopt the structure according to the thermodynamic equilibrium, which also depends on the crystallites size [35].

Zhang et al. [9] investigated nickel catalysts (Ni/CeO_2) with different size of nickel crystallites and they found that nickel nanoparticles have different catalytic activities in the steam reforming of ethanol, depending on the nickel crystallites size. The size of nickel particles has the crucial significance. If nickel particles are smaller the catalysts exhibit better catalytic properties. The Ni/CeO_2 catalyst with smaller nickel crystallites showed a better activity, stability and a higher resistance to sintering and formation of carbon deposits in the SRE process than the catalysts with larger nickel crystallites. The conclusions presented in that paper are comparable to those contained in our paper. They confirm that the smaller nickel crystallites are the better catalytic properties of the catalyst in the SRE process are.

Van Hardeveld and Hartog in their work [36] presented the results of many computational studies describing the arrangement of atoms in small metal particles. Among others, they presented the face centered cubic (fcc) octahedron model of nickel particle. In that Ni particle model, three types of surface atoms are distinguished: face atoms, edge atoms and corner atoms. The ratio of the number of low-coordinated

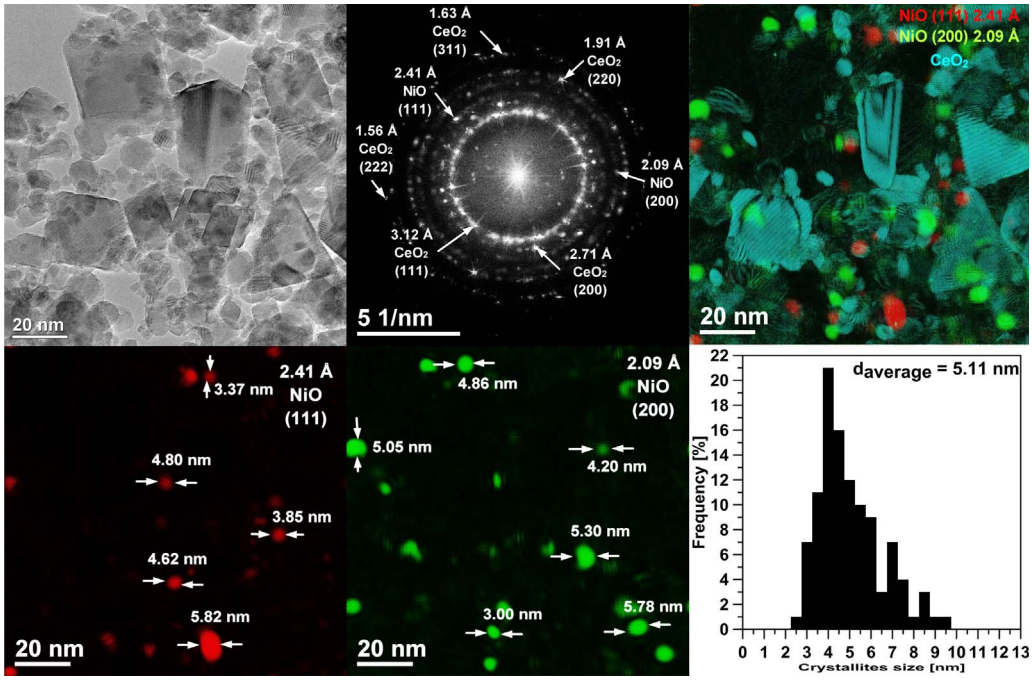

Fig. 6. HRTEM image, FFT with phase identification and NiO crystallites size distribution in the fresh KNi/CeO_2 catalyst.

surface atoms to the number of surface atoms has been calculated. The surface plane atoms fraction reached 90% for particles 6 nm and dropped to zero for particles about 0.6 nm in which all atoms were located at the edges and at the corners. The influence of coordination of surface atoms was pronounced for particles smaller than 4 nm, where the largest (~ 100%) share of corner atoms in the particle was obtained. When the particle size increased (> 4 nm), the contribution of the corner atoms decreased drastically, thus increasing the contribution of the face atoms and to a small extent the contribution of the edge atoms. For particles > 10 nm, the negligible fraction of corner atoms in the total number of surface atoms, the high (80%) share of face atoms and the decreasing share of edge atoms were observed.

The similar situation was observed when the nickel particle was compared to the fcc cubo-octahedron. For that Ni particle model five types of surface atoms were identified: corner atoms, two types of edge atoms and two types of face atoms (111) and (100). For particles < 4 nm, the maximum number of corner atoms in the total number of surface atoms was obtained. When the nickel particle size increased (> 4 nm), then the contribution of corner atoms drastically decreased and the share of face atoms (111) increased. The maximum share of edge atoms in the total number of surface atoms was obtained for 6 nm particles, above this size, the share of the edge and corner atoms decreased and the share of the faces atoms (111) and (100) increased. The maximum share of faces atoms (111) and (100) was obtained for particles above 25 nm.

Changes in the different proportions of surface atoms are also related to changes in the electronic characteristics. It has been also found that the catalytic properties of a metal depend on the contribution of individual types of atoms to the total number of surface atoms.

When the size of nickel particles increases the ratio between face atoms and total surface atoms also increases, while the ratios between corner atoms and total surface atoms as well as edge atoms and total surface atoms decrease. In consequence, a positive size effect is observed for reactions that have a tendency to occur on lower-coordinated sites such as corner atoms and edge atoms, while a negative size effect is observed for reactions that occur more rapidly on face atoms. The first of the cases corresponds to positive structural sensitivity, and the second one to negative structural sensitivity. If the catalysis is preferred by low coordination atoms, small particles give higher reaction rates, while the catalysis is favored by face atoms, large particles would then give higher reaction rates. Thus, the catalysis of certain reactions requires specific places of surface atoms.

The size of the metal particles affects the contribution of individual active sites (faces, edges, terraces or corners) on the particle, and this in turn affects the activity of the active phase in the process. The increase in the particles size of the active phase simultaneously increases the share of faces and decreases the share of edges on the surface of metal particles. On the other hand, decreasing of the metal particles will increase the proportion of atoms on edges and reduce the share of atomic faces on the metal particle. A change of the ratio of different active centres on the particles affects their activity in the catalytic reaction [25–27,37,38]. Hence, different crystallites size of the nickel active

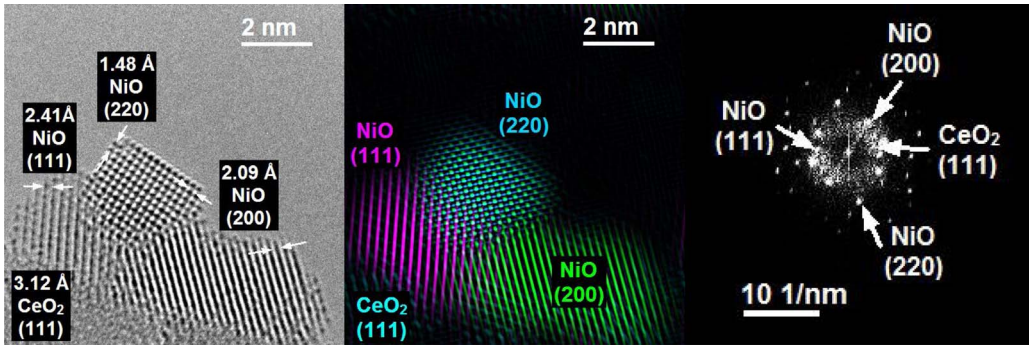

Fig. 7. HRTEM image and FFT with phase identification of the fresh KNi/CeO_2 catalyst.

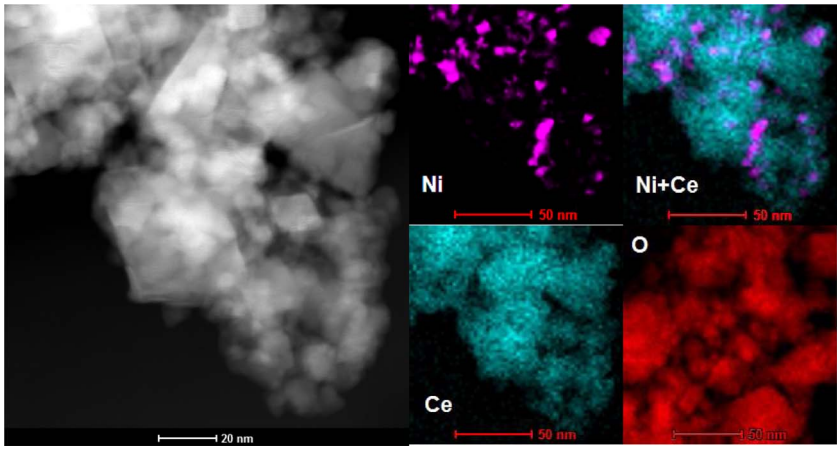

Fig. 8. STEM-EDS analysis of the Ni/CeO_2 catalyst reduced at 420 °C.

phase observed in our activated (reduced) Ni/CeO_2 and KNi/CeO_2 catalysts can significantly affect the activity, selectivity and stability of these systems in the SRE, through the participation of various active centres in the reaction.

Based on the results presented in this work it was shown that potassium promoted and unpromoted nickel catalysts exposed identical crystallographic planes and face centered cubic structure. Therefore, we cannot suggest that differences in the activity, selectivity and stability of catalyst in the SRE depend on crystallographic planes existed in the nickel active phase. These differences may result from the size of different nickel crystallites in both catalysts and presence of potassium in one of them. The unpromoted nickel catalyst contains nickel crystallites of about 3-3.5 nm, what indicates, as it is suggested in the work [36], that such nickel crystallites contain a significant contribution of edge atoms, lower share of corner atoms and low share of face atoms in the total number of surface atoms (edge atoms > corner atoms > face atoms). While in case of potassium promoted nickel catalyst with average nickel crystallites size about 8.1–8.4 nm, there is a high share of face atoms, low share of edge atoms and very low share of corner atoms (face atoms > edge atoms > corner atoms). The various shares of different surface atoms (face, edge, corner) can responsible for the different selectivity of the SRE on the nickel catalysts, as show in Fig. 17. The most significant is its influence to the coke formation.

The structural sensitivity of the SRE reaction on nickel catalysts presented in this work has distinct influence on their stability and activity. As can be seen from the results (Fig. 17 and Table 1), the unpromoted nickel catalyst with small nickel crystallites is much more stable in the steam reforming of ethanol than the potassium promoted nickel catalyst with large nickel crystallites. Large nickel crystallites contribute to the production of significant amounts of carbon deposits which accelerate deactivation of the catalyst and worsen its stability in the process. On the other hand, on the small nickel crystallites, small amounts of carbon deposits are formed and hence the catalyst is more stable and longer holds high activity in the process. On this basis it can be stated that the steam reforming of ethanol on nickel catalysts is a structurally sensitive reaction.

3.2. X-ray studies of crystallites size

The average crystallites sizes of nickel active phase determined by

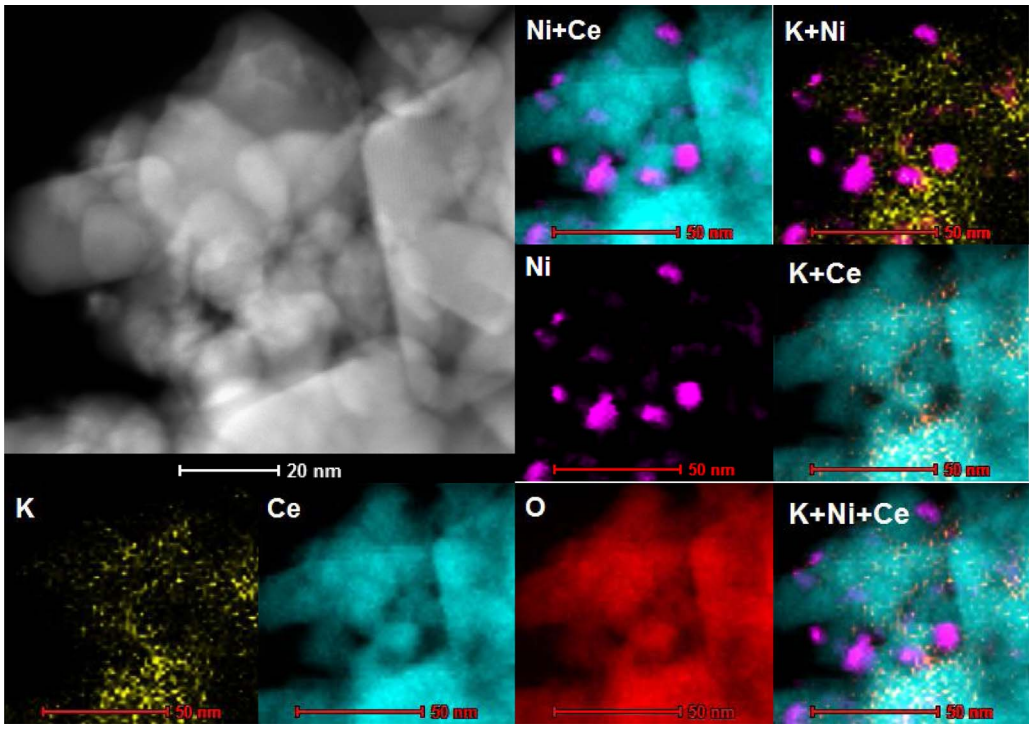

Fig. 9. STEM-EDS analysis of the KNi/CeO_2 catalyst reduced at 420 °C.

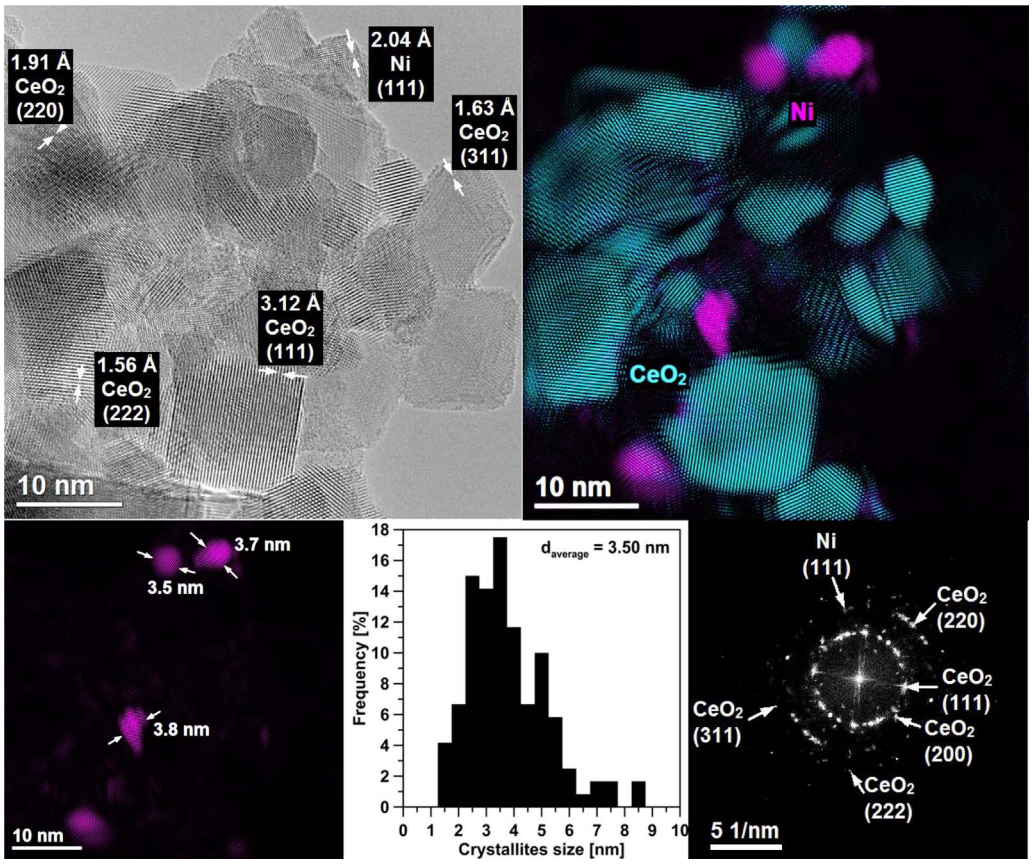

Fig. 10. HRTEM image and FFT with phase identification of reduced Ni/CeO_2 catalyst and nickel crystallites size distribution.

the XRD measurements (Fig. 13) are presented in Table 1. Nickel oxide crystallites size in both unpromoted and potassium promoted catalysts are compared with those obtained from TEM measurements. The XRD measurements showed that in the case of the KNi/CeO_2 catalyst the crystallites size of the nickel active phase in the NiO form is much smaller than the crystallites size of metallic form (reduced at 420 °C). The reduction of the KNi/CeO_2 catalyst causes an increase in the crystallites size of the active phase from 5.6 nm for nickel oxide (NiO) to 9.3 nm for metallic nickel form (Ni^0). Any such significant change in the crystallites size was not found for the unpromoted Ni/CeO_2 catalyst. The NiO crystallites size of the fresh Ni/CeO_2 catalyst was 5.0 nm while reduction at 420 °C forms Ni^0 crystallites with the size of 5.8 nm.

The X-ray diffraction is a simple and rapid analysis; however, the results obtained for reduced catalysts are inconsistent with those from TEM measurements – the XRD-obtained crystallites sizes are not accurate. These differences in the crystallites size may result from inherent limitations in the peak profile analysis of the XRD data and with application of a width of the peak at the half of its maximum, what excludes very small crystallites from XRD data analysis [4,21,39].

3.3. Hydrogen chemisorption

The total hydrogen chemisorption isotherms over Ni/CeO_2 and KNi/CeO_2 catalysts reduced at 420 °C were measured in the temperature range from 40 °C to 140 °C or 160 °C (Fig. S4). When the temperature increased the isotherms became linear at lower equilibrium pressures for both catalysts. The amount of adsorbed hydrogen increased initially. Then it goes through a maximum and finally it decreases a little at the highest temperatures. In each experiment two adsorption isotherms were measured. The first of isotherms includes the total hydrogen adsorption while the latter includes the weak hydrogen adsorption. The difference between total and weak adsorption isotherms contributes the amount of a strong hydrogen adsorption on the catalysts [40].

The amounts of the total and weak hydrogen chemisorbed and the difference between both hydrogen chemisorptions i.e. strongly chemisorbed hydrogen, at each measurement temperature, for unpromoted and potassium-promoted nickel catalysts are presented in Fig. 14. For both studied catalysts, the increase of the total, weak and strong hydrogen chemisorption increase simultaneously with the temperature in the lower temperatures range. The maximum of the total hydrogen chemisorption was recorded at 110 °C for the Ni/CeO_2 catalyst and at 120 °C for the KNi/CeO_2 catalyst. For the strong hydrogen chemisorptions, the maximum of hydrogen uptake was observed at 100 °C for both catalysts. A small decrease of the total and very clear decrease of strongly adsorbed hydrogen amounts were observed above the temperatures of maxima of hydrogen chemisorption. In the whole range of temperatures, the weak hydrogen chemisorption increased almost linearly. It should be noticed that the uptake of hydrogen (total, strong and weak) at every temperature is much lower on the potassium-promoted catalyst than that in the case of the unpromoted Ni/CeO_2 catalyst – the potassium promoter strongly diminishes chemisorption of hydrogen.

In Fig. 15 the average crystallites size of the nickel active phase determined (calculated) from the total and strong hydrogen adsorption for Ni/CeO_2 and KNi/CeO_2 catalysts is presented. Based on the strongly chemisorbed hydrogen uptake, the lowest crystallites sizes, 4.5 nm for the Ni/CeO_2 catalyst and 15 nm for the KNi/CeO_2 catalyst were obtained for 100 °C. Above and below of that hydrogen chemisorption temperature, the calculated nickel crystallites sizes are much larger. For the total amount of chemisorbed hydrogen, the lowest average crystallites size of the nickel active phase (3.0 nm) in the case of Ni/CeO_2 catalyst was calculated on the basis of the hydrogen chemisorption uptake obtained at 110 °C. In the case of the KNi/CeO_2 catalyst, the smallest average size of nickel crystallites (8.10 nm) was determined when the total hydrogen chemisorption data measured at 120 °C were used. At lower temperatures, the average crystallites sizes calculated

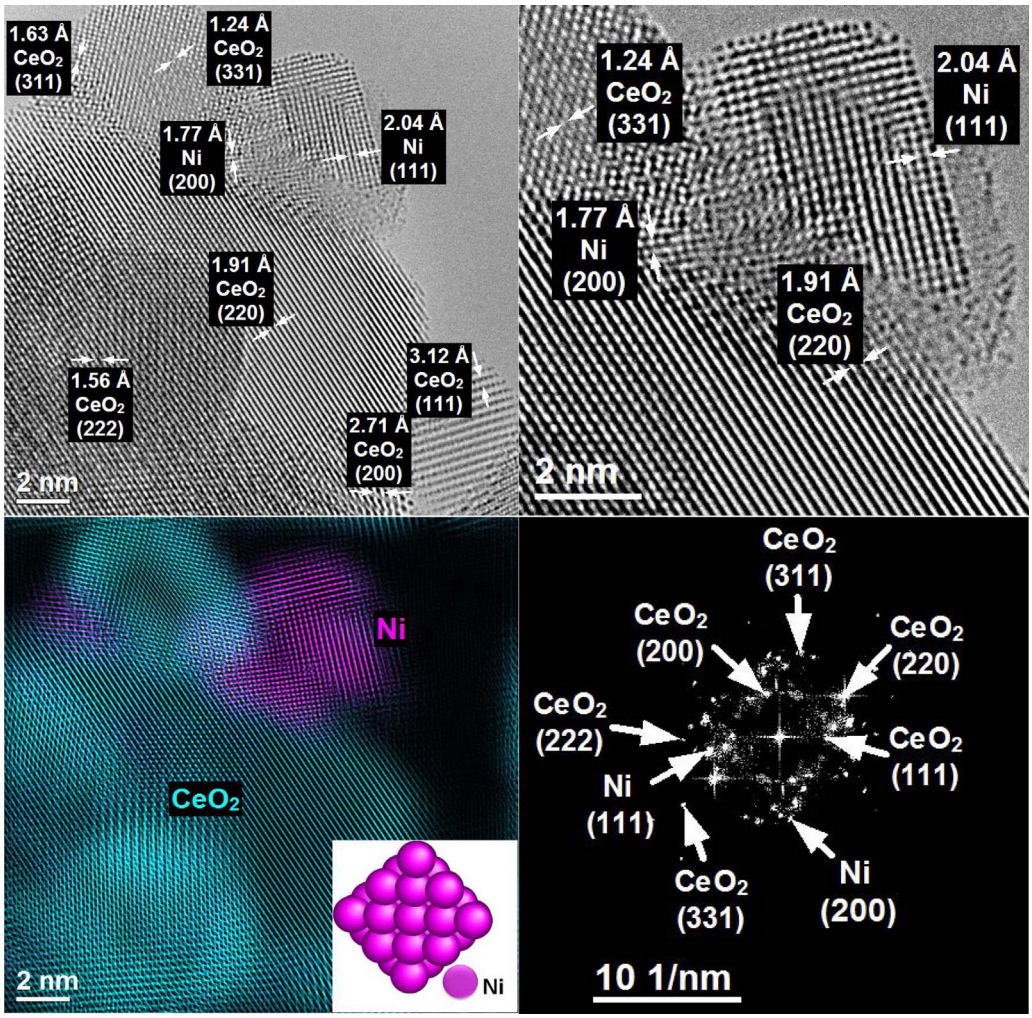

Fig. 11. HRTEM image and FFT with phase identification of reduced Ni/CeO_2 catalyst.

from the total hydrogen chemisorption are much higher for both nickel catalysts.

The comparative studies presented in Table 1 on determination of the average nickel crystallites size by TEM, XRD and hydrogen chemisorption show very comparable results obtained from electron microscopy and hydrogen chemisorption, when the total hydrogen chemisorption data obtained at 110 °C for the Ni/CeO_2 catalyst or at 120 °C for the KNi/CeO_2 catalyst are used for determination of the dispersion of the nickel active phase. The hydrogen chemisorption analysis shows that the higher temperature of hydrogen chemisorption is necessary to obtain the proper average crystallites size of the nickel active phase for the catalyst with potassium promoter. Nevertheless, despite that the average crystallites size calculated from the total hydrogen chemisorption is higher at higher temperatures, it does not differ significantly above 110 °C (Ni/CeO_2) and 120 °C (for the KNi/CeO_2) till 140 °C.

Presented results also clearly proved that the average crystallites sizes of the nickel active phase calculated from strongly chemisorbed hydrogen uptakes are overestimated.

3.4. H_2-TPR

The H_2-TPR studies (Fig. 16) show that for the unpromoted and potassium-nickel catalysts with the ceria support several NiO reduction peaks are observed. Du et al. [41] suggested two-step reduction of NiO species on the ceria support. According to that studies the first reduction peak at 265–285 °C comes from reduction of NiO species weakly interacting with the CeO_2 support while the second peak, at 360 °C–380 °C, was attributed to reduction of NiO species strongly interacting with the CeO_2 support [41].

In our studies it can be suggested that for the KNi/CeO_2 catalyst, the reduction peaks at 281 °C and 291 °C result from reduction of low-dispersed crystallites of NiO (different reducible) weakly interacting with the CeO_2 support, and peaks at 305 °C and 314 °C can be attributed to reduction of nickel oxide strongly interacting with the CeO_2 support, highly dispersed crystallites and clusters of NiO (different reducible) [41,42]. The peaks at 138 °C and 251 °C may be attributed to reduction of the surface adsorbed oxygen species [41].

For the Ni/CeO_2 catalyst, two reduction peaks at 264 °C and 312 °C come probably from reduction of weakly interacting with the CeO_2 support, lower dispersed crystallites and clusters of NiO (different reducible). The next two peaks observed at 360 °C and 395 °C reflect probably reduction of highly dispersed crystallites and clusters of NiO (different reducible) strongly interacting with the CeO_2 support [41,42]. The range of 120–229 °C we assigned to reduction of surface adsorbed oxygen species [41].

The difference in the amount of peaks in TPR profiles of Ni/CeO_2 and KNi/CeO_2 catalysts can be caused by the fact that the addition of the potassium promoter shifts the reduction of nickel active phase towards the lower temperatures, and as a result of the shifting some of the peaks identified for the Ni/CeO_2 catalyst can be overlapped in the case of the KNi/CeO_2 catalyst.

In the case of the CeO_2 support alone (Fig. 16), Luo et al. [43] reported that the H_2-TPR profile of CeO_2 shows two reduction peaks. The first peak, at 528 °C, they attributed to reduction of surface oxygen species (capping oxygen) and the second peak, at 820 °C, to reduction of the bulk CeO_2 (according to the reaction $2CeO_2 + H_2 \rightarrow Ce_2O_3 +$

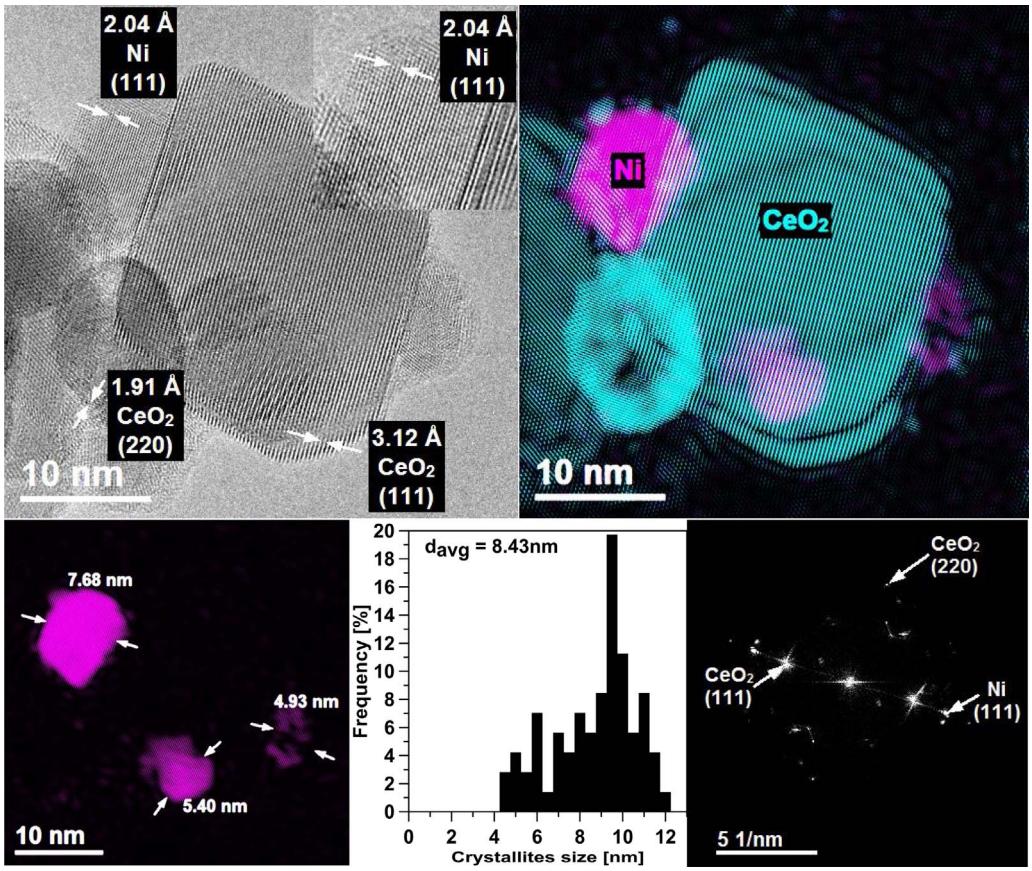

Fig. 12. HRTEM image and FFT with phase identification of reduced KNi/CeO_2 catalyst and nickel crystallites size distribution.

H_2O, $Ce^{4+} \rightarrow Ce^{3+}$) [44,45]. For the CeO_2 support of both catalysts we observed three reduction peaks. Based on work Luo et al. [43] it can be concluded that two peaks, at 345 °C and 418 °C, come from reduction of surface oxygen species and the surface of CeO_2 crystallites, while the peak at 800 °C can be attributed to reduction of the bulk of CeO_2. In the case of catalysts, reduction peaks below that latter temperature we relate to overlapped reduction of both, NiO and ceria [41] phases, because when Ni^{2+} ions are reduced into metallic nickel at the Ni—O—Ce interface structure, then also Ce^{4+} ions are reduced into Ce^{3+} ions. The TPR process involves also partial reduction of the CeO_2 support as hydrogen is consumed in excess to that necessary for reduction only all amount of nickel oxide present in the catalyst. Similar effect and its explanation were reported in [42,46].

On the basis of above results it can be concluded that the complete reduction of NiO crystallites is observed in the KNi/CeO_2 catalyst at lower temperature (314 °C) than it was observed for the unpromoted Ni/CeO_2 catalyst (395 °C). The addition of the potassium promoter to the nickel catalyst decreased the reduction temperature of the nickel active phase (NiO). It can be caused by the higher share of less dispersed crystallites and clusters of NiO, weakly interacting with the CeO_2 support in the KNi/CeO_2 catalyst and the higher share of highly dispersed crystallites and clusters of NiO strongly interacting with the CeO_2 support in the case of the Ni/CeO_2 catalyst.

3.5. Steam reforming of ethanol over unpromoted and potassium-promoted nickel catalysts

The steam reforming of ethanol on Ni/CeO_2 catalyst with fcc (face centered cubic) nickel crystallites was studied by Xu et al. [5]. They found that the active components of the catalyst under steam reforming condition include metallic Ni and Ce^{3+}. In the steam reforming of ethanol process, it was shown that Ni helps in the adsorption of the ethanol and in the cleavage of its C − C bond, while Ce^{3+} facilitates the decomposition of water with the subsequent generation of OH groups which are essential for reacting with C_xH and C_yO_zH and produce H_2 and CO_2. The reaction pathway leads to H_2 and CO_2 predominantly via the formation of ethoxy, acetate, and carbonate surface species.

Fig. 17A shows conversion of ethanol and water over Ni/CeO_2 and KNi/CeO_2 catalysts during 100 h catalytic tests in the steam reforming of ethanol. Initially (from 0 to 30 h), both catalysts ensure 100% conversion of ethanol. After 30 h, only Ni/CeO_2 catalyst indicates 100% conversion of ethanol, while the conversion of ethanol over KNi/CeO_2 catalyst decreases to 70% in the final stage of the test. Similar changes were observed in the case of water conversion (water is in the excess in

Table 1
Average size of crystallites of nickel active phase in fresh, reduced and used (in the SRE) Ni/CeO_2 and KNi/CeO_2 catalysts, determined by TEM, XRD and hydrogen chemisorption methods.

Catalyst	TEM [nm]			XRD [nm]		H_2 chemisorption [nm]
	fresh	reduced	after SRE	Fresh	reduced	reduced
Ni/CeO_2	4.90 ± 0.25	3.50 ± 0.18	4.95 ± 0.25	5.00 ± 0.25	5.80 ± 0.29	3.00 ± 0.21*
KNi/CeO_2	5.11 ± 0.26	8.43 ± 0.42	5.90 ± 0.30	5.60 ± 0.28	9.30 ± 0.47	8.10 ± 0.57**

Measured at *110 °C/**120 °C.

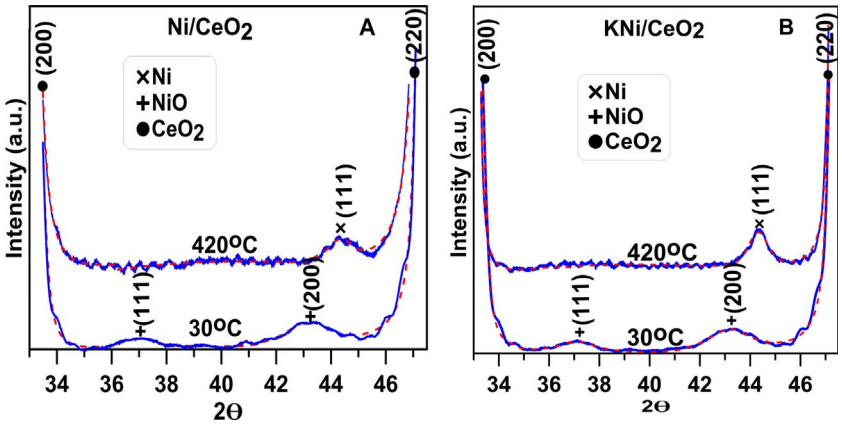

Fig. 13. XRD patterns of (A) Ni/CeO_2 and (B) KNi/CeO_2 catalysts taken at 30 °C (fresh, oxide form) and at 420 °C after in situ reduction with hydrogen.

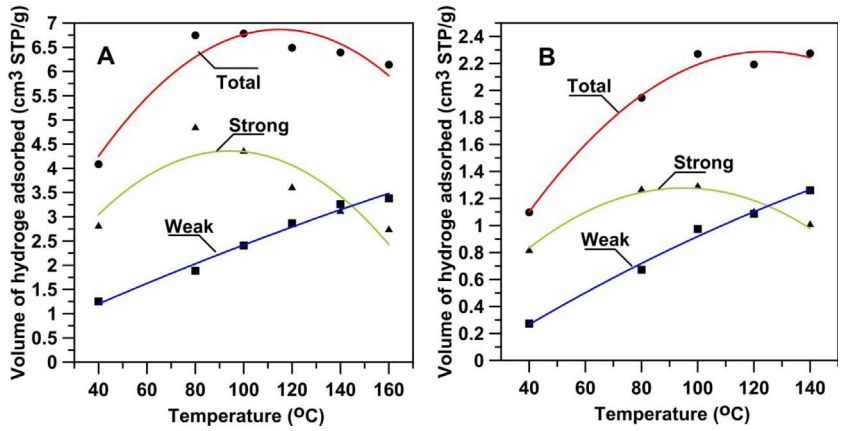

Fig. 14. Total, weak and strong hydrogen chemisorption measured at various temperatures over (A) Ni/CeO_2 and (B) KNi/CeO_2 catalyst reduced in situ at 420 °C.

relation to the reaction stoichiometry). The conversion of water over KNi/CeO_2 catalyst decreases from 20% after 30 h to 10% after 100 h of the SRE test. Over Ni/CeO_2 catalyst the conversion of water slowly increases from 12 to 18%.

The selectivity (Fig. 17B) of hydrogen formation over Ni/CeO_2 catalyst increases from 68% to 75% after 100 h, whereas the selectivity of the SRE towards carbon dioxide increases from initial 58% to 60% after 100 h. The selectivity to CH_4 decreases from 41% to 35%.

Over KNi/CeO_2 catalyst the selectivity of the steam reforming of ethanol to hydrogen decreases from 85% to 55% after 100 h of test (Fig. 17C). Similarly, the selectivity towards carbon dioxide decreases from 72% to 40% after 100 h of the SRE. The decreasing of the selectivities to H_2 and CO_2 after 30 h takes place at the same time with an increase in the selectivity towards acetaldehyde CH_3CHO. The unpromoted nickel catalyst generated only minor amounts of CH_3CHO, in contrast to the potassium promoted nickel catalyst. The addition of potassium to the Ni/CeO_2 catalyst leads to noticeable decrease of methane production. Both catalysts generate small amounts of carbon monoxide what is an important feature taking into account a potential application of these catalysts for production of hydrogen for fuel cells; CO is undesirable product because PEM fuel cells are sensitive to poisoning by it [47–49].

Decreasing of the ethanol and water conversion as well as selectivities to H_2 and CO_2 over KNi/CeO_2 indicates that the catalyst undergoes progressive deactivation during the SRE process under applied conditions. The most likely the reason of the catalyst deactivation is production of carbonaceous deposit on the catalyst surface during the ethanol conversion process. Nickel catalysts are known from the tendency to production of carbon deposits in the steam reforming of ethanol [50,51]. On the basis of results presented in Fig. 17, it can be

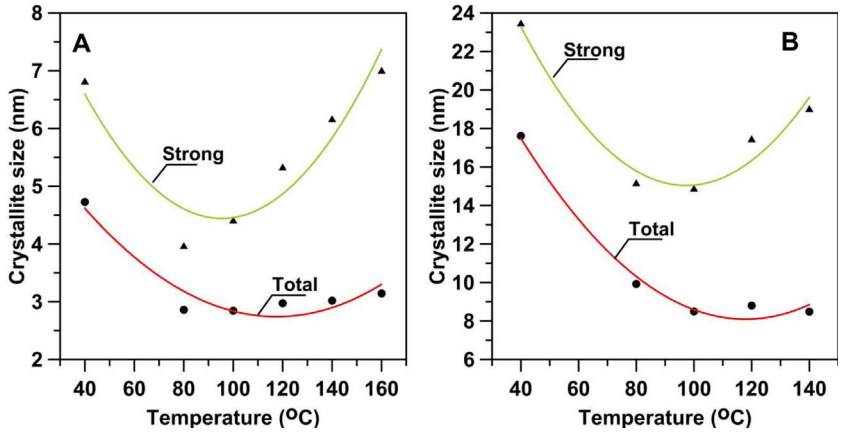

Fig. 15. Calculated average crystallites size of the nickel active phase in (A) Ni/CeO_2 and (B) KNi/CeO_2 catalysts determined (calculated) from the total and strong hydrogen chemisorption data obtained at various temperatures.

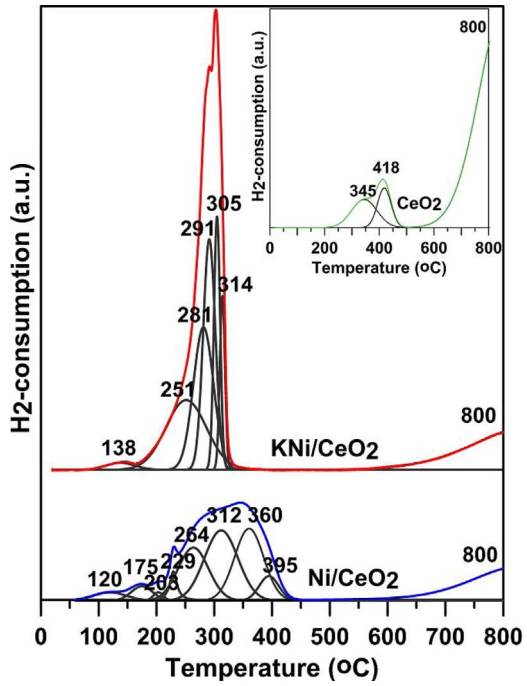

Fig. 16. H_2-TPR of nickel catalysts with ceria support (without and with potassium promoter) and H_2-TPR of ceria support (inset).

considered that one of the reasons of formation of carbonaceous deposits and deactivation of catalysts is production of acetaldehyde. Ethanol can undergo dehydrogenation to CH_3CHO (acetaldehyde) according to the reaction $C_2H_5OH \rightarrow CH_3CHO + H_2$ [3–5,47,52]. Next, acetaldehyde can undergo aldol condensation and finally carbonaceous deposits ($CH_3CHO \rightarrow$ aldol condensation $\rightarrow$ carbon) can be formed that deactivate the catalyst during the SRE process [4,6]. Another reason of catalysts deactivation could be production of methane and carbon monoxide, because the former can be decomposed to carbonaceous deposit, according to reaction $CH_4 \rightarrow C + 2H_2$ while CO can left carbon on the catalyst surface due to the Boudouard reaction $2CO \leftrightarrow C + CO_2$ [3,5,6,53,54].

The worse stability of the SRE over the potassium-promoted catalyst seems rather unexpected as potassium promoter is frequently applied for increasing resistance of catalysts to coking and, therefore, for improving the stability of the SRE process. Different stability of reactants conversion and selectivity to different products in the steam reforming of ethanol over unpromoted and potassium-promoted nickel catalysts can be related to different crystallites size of the nickel active phase in both catalysts. Crystallites with different sizes are accompanied by participation of various active centres (face, edges, steps, terraces and corners − mentioned in the section 3.1) on nickel particles, taking part in formation of different reaction products in the SRE process. Smaller crystallites of the nickel active phase (in the unpromoted Ni/CeO_2) favour stability of the catalyst and its selectivity to the most desirable reaction products (H_2 and CO_2), while large nickel crystallites in the potassium-promoted KNi/CeO_2 result in the worse stability of the catalyst system and production of undesirable reaction products. Therefore, the unpromoted Ni/CeO_2 catalyst with smaller nickel crystallites shows better stability and selectivity in the conversion of ethanol than the potassium-promoted KNi/CeO_2 catalyst with larger nickel crystallites.

3.6. Characterization of catalysts used in the steam reforming of ethanol

Frusteri et al. [15] compared the catalytic and structural properties of the potassium promoted and unpromoted nickel catalysts in the steam reforming of ethanol. It was shown that both catalysts containing comparable in respect of the size crystallites of the active phase (in the fresh form), produced similar amounts of carbon and showed comparable selectivity to gaseous reaction products, but they had different activity in the SRE. Potassium-promoted nickel catalyst showed better activity in the SRE than unpromoted nickel catalyst. However, the activity of both catalysts decreases during their work in the reaction. Similar results can be also found in the work [55].

The STEM-EDS analysis of the Ni/CeO_2 catalyst after steam reforming of ethanol (Fig. 18) shows that it was covered by a large amount of carbon deposit. The carbon deposit formed during the reaction pushed part of the nickel active phase from the ceria support while the rest part of nickel still remained on the support surface.

The distribution of the nickel crystallites size in the Ni/CeO_2 catalyst after its work in the SRE is presented in Fig. 18. The average nickel crystallites size obtained on the basis of the STEM-EDS analysis is 4.95 nm and it was larger than that in the freshly reduced Ni/CeO_2 catalyst (3.50 nm, Table 1).

Fig. 19 shows STEM-EDS analysis of the KNi/CeO_2 catalyst after SRE. Similar to the Ni/CeO_2 catalyst, the KNi/CeO_2 catalyst is covered by large amounts of carbon deposits and parts of the nickel active phase is pushed from the support by carbon deposits formed during the reaction, whereas the rest of nickel still remains on the ceria support. The EDS maps (K + Ce, K + Ni and K + Ni + Ce) of KNi/CeO_2 catalyst after SRE reaction show that the significant amount of potassium promoter is located on the ceria support while the remaining promoter is located on the nickel active phase deposited on the catalyst. The K + Ni EDS map also indicate that nickel which is pushed from the ceria support does not contain potassium on their surface or its very small amount is present on the nickel surface but it is not detected by EDS analysis. The EDS maps show also noticeable agglomeration of potassium species.

The chemistry aspects of the potassium promoter and its bonding to the catalysts active phase and support were discussed in the literature. Bengaard et al. [56], Murray et al. [57] and Finetti et al. [58] showed that potassium promoter in the nickel catalyst is bonded to the surface of nickel active phase by oxygen atoms. Ogo et al. [33] found the presence of amorphous layer of potassium oxides on the surface of potassium-promoted catalysts designed to the steam reforming of ethanol. Also, recent work of Turczyniak et al. [59] describes insightful

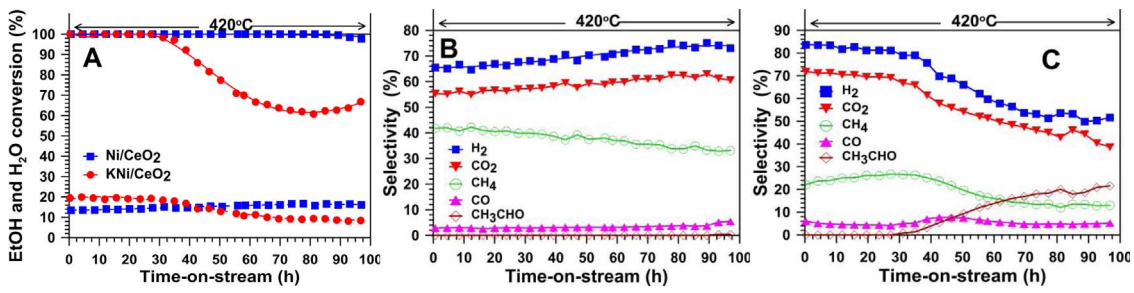

Fig. 17. (A) Conversion of ethanol and water over Ni/CeO_2 and KNi/CeO_2 catalysts, selectivity of Ni/CeO_2 (B) and KNi/CeO_2 (C) catalysts in the steam reforming of ethanol (EtOH/H_2O=1/12 mol/mol, 420 °C).

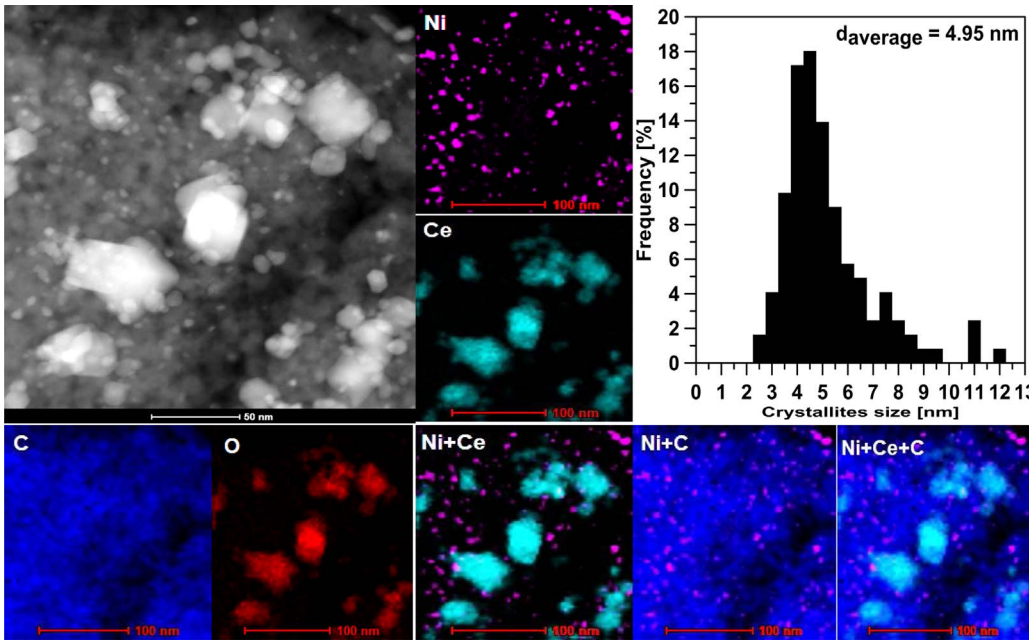

Fig. 18. STEM-EDS analysis of Ni/CeO_2 catalyst after steam reforming of ethanol and nickel crystallites size distribution.

chemistry of potassium promoter in the SRE cobalt catalysts. They showed that the surface of potassium-promoted catalysts is covered by the amorphous layer of potassium oxides. The XPS analysis of reduced potassium-promoted catalyst and its surface after SRE showed that most probably both metal active phase particles and ceria support were covered by potassium bonded to oxygen layer (K-O). These sites (K-O) were recognized as playing promoting role in the SRE, providing an additional oxygen-containing species reservoir. It was found that a higher concentration of K-O sites is required for hindering of carbon deposition on the catalyst. Small concentration of K-O sites leads to high production of carbon deposits on the catalysts, with formation completely (or almost completely) dehydrogenated C=C type carbonaceous deposit, in a large part as graphitic fibrous and layers. For total elimination of carbon deposition phenomena, the high abundance of K-O sites is required [59].

When the fibrous carbon deposit is produced during the SRE reaction, the metal active phase with potassium promoter is pushed from the ceria support, carried and crushed by the carbon deposits. In this way small particles of destroyed active metal with/without potassium promoter are sunk in the carbon deposit. The loss of small particles (< 2 nm) of nickel active phase in the carbon deposit was also presented in the work [5]. When the active metal particles over the time lose all or some part of potassium promoter from the surface, it starts to function as a metal without potassium or with very small amounts of potassium on the surface. Therefore, EDS maps present for KNi/CeO_2 catalyst do not show potassium promoter on the nickel active phase or show its very small amounts. Such small amounts of potassium are very difficult to detect by EDS analysis.

The nickel crystallites size in the used KNi/CeO_2 catalyst were measured by using STEM imagining coupled with EDS analysis and the average size of nickel crystallites was 5.90 nm (Fig. 19), which means that the average crystallites size decreased from initial 8.43 nm to 5.90 nm after SRE. It proves that original nickel crystallites underwent defragmentation by growing carbonaceous deposit under SRE conditions. In some cases, when a growing filamentous carbon contains nickel crystallites, two or more carried crystallites can form a larger cluster what led to formation of large (thick) carbon nanotubular structures. However, the phenomenon of carrying of the nickel active phase crystallites by the carbon deposit may be also accompanied by its gradual detachment and losing in the carbon deposit. The growth of crystallites of nickel and their redispersion by carbon deposits formed during the reaction can be a reason of the change in the range of crystallites size in both catalysts in comparison with the crystallites size range of freshly reduced catalysts (Figs. 18 and 19).

Fig. 20 shows identification of crystal phases in the Ni/CeO_2 catalyst used in the SRE reaction. Based on the HRTEM images of the Ni/CeO_2 catalyst and FFT generated from the image, the active phase after reaction was observed as metallic nickel with characteristic crystallographic orientation (111). The crystal structure of nickel remains unchanged under SRE conditions and it agrees very well to the Fm3 m space group and the cubic crystal lattice. In the HRTEM images fragments of the ceria support with the crystallographic orientation (111) were also found. Both, the nickel active phase and the ceria support are surrounded by amorphous and graphite (with crystallographic orientation (002)) carbon deposits.

The microscopic characteristics of the KNi/CeO_2 catalyst by HRTEM and FFT (Fig. 21) after its work in the steam reforming of ethanol, enables identification and separation of phases present in that catalytic system. The nickel active phase in the used KNi/CeO_2 catalyst was observe as metallic nickel with crystallographic orientations (111), (200); i.e. remained as unchanged cubic crystal lattice corresponding to the Fm3 m space group. The carbon deposit formed during the reaction created amorphous and graphite structure with crystallographic orientation (002).

The electron microscopy results presented in Figs. 20 and 21 also show that the nickel active phase remains in metallic form in the SRE. The conditions of the SRE process do not affect the form in which nickel is present just after the reduction. It suggests that metallic nickel has good resistance in the oxidizing conditions occurring during the process.

The stability of the catalytic system depends also on the amount and on the type of carbonaceous deposit formed on its surface during the SRE reaction. A good view on amounts and kinds of carbon deposits produced during the SRE reaction on Ni/CeO_2 and Ni/CeO_2 catalysts after 24 h and 100 h provided SEM images shown in Fig. 22. On the Ni/CeO_2 catalyst small amounts of short and thin fibrous carbon deposit produced on its surface during 24 h in the SRE is observed. After 100 h in the SRE two types of fibrous carbon deposits on the Ni/CeO_2 catalyst are observed. The first type of fibrous carbon deposit is long and thick; HRTEM images (Fig. 23) proved that it has an amorphous (disordered) structure. The carbonaceous fibres of the second type are short and thin with mostly graphite structure (Fig. 23). In the case of the potassium-

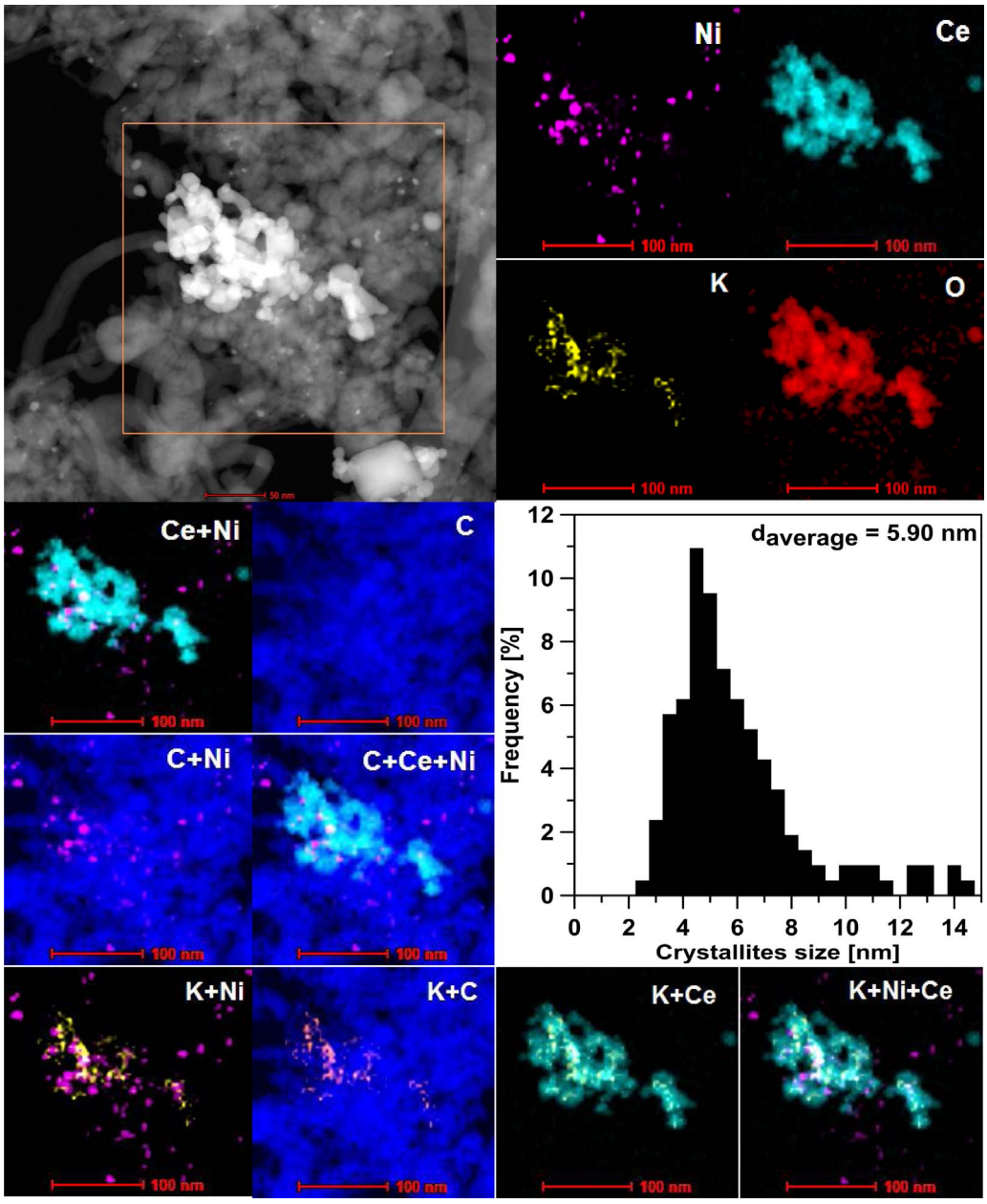

Fig. 19. STEM-EDS analysis of KNi/CeO_2 catalyst after steam reforming of ethanol and nickel crystallite size distribution.

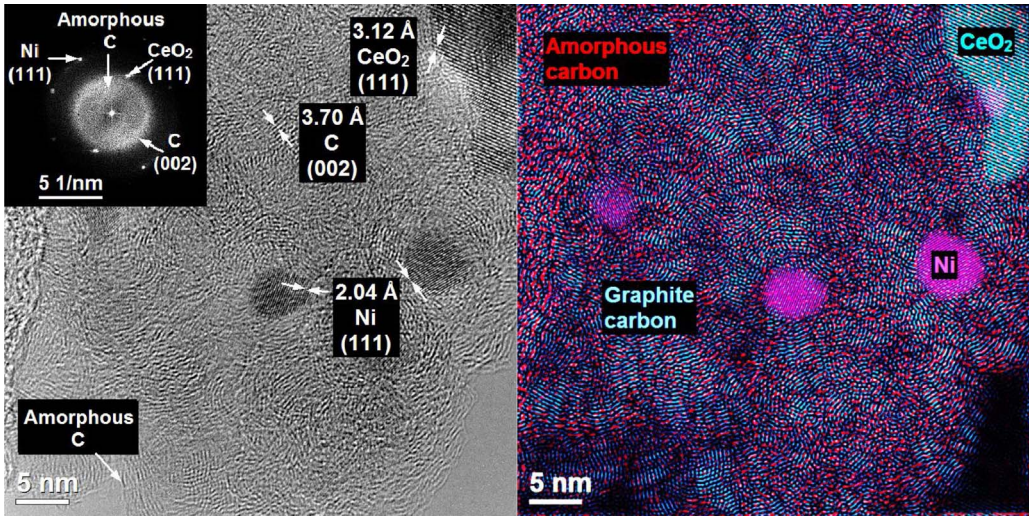

Fig. 20. HRTEM images of Ni/CeO_2 catalyst after steam reforming of ethanol.

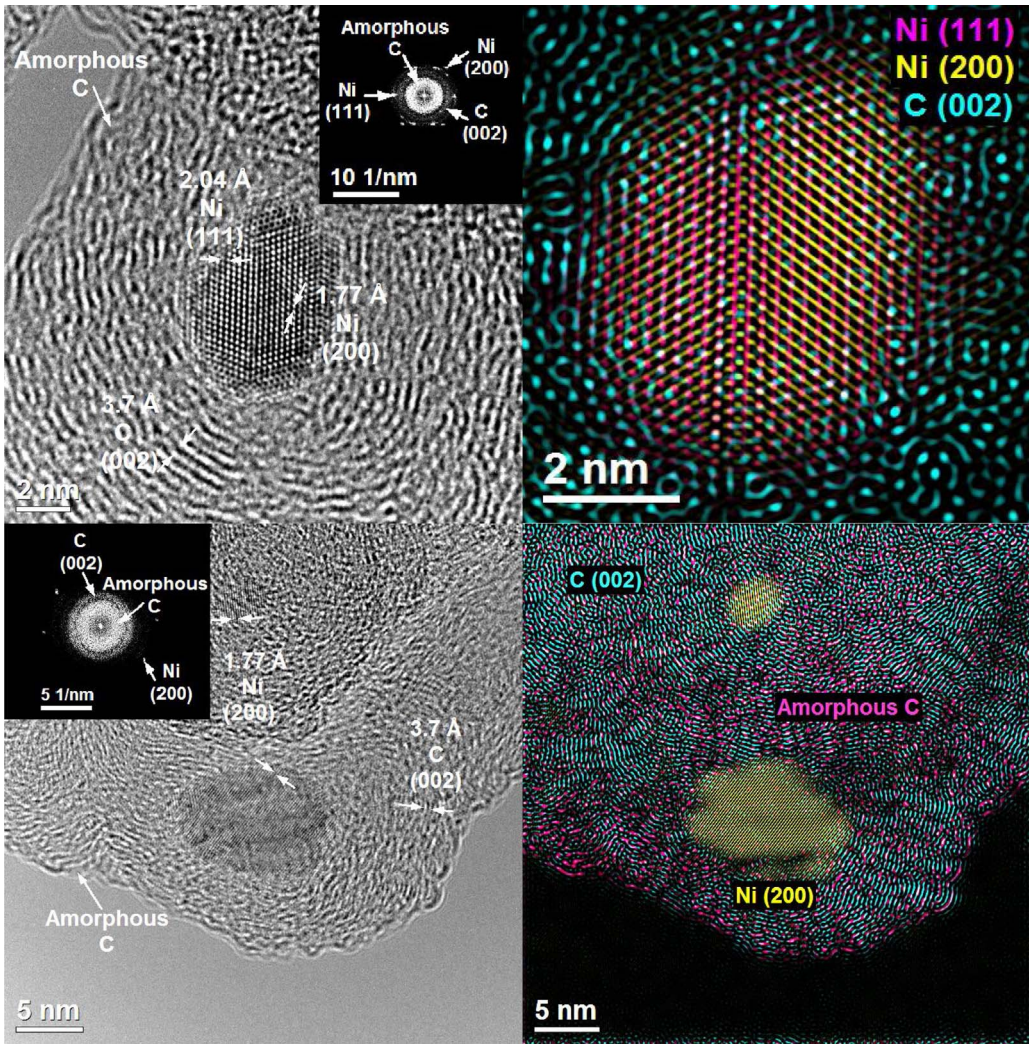

Fig. 21. HRTEM images of KNi/CeO_2 catalyst used in the steam reforming of ethanol.

promoted KNi/CeO_2 catalyst, after 24 h quite large amount (much larger than on the Ni/CeO_2 catalyst) of thin and long fibrous carbon deposit is observed; the length and diameter of fibres is much larger (already after 24 h of the SRE) than in the case of the unpromoted nickel catalyst. After 100 h in the SRE, on the KNi/CeO_2 catalyst only very large amounts of long and medium-thick fibrous carbon deposits with graphitic (ordered) structure, similar to shown in right image of Fig. 23, were found.

An additional, macroscopic insight into nature of carbonaceous deposits present in the used catalysts gave their Raman spectra (Fig. 24). Although observed Raman shift of some Raman bands varies with laser wavelength they are essentially independent of the type of carbon [60]. The nature of deposits in both catalysts is similar. According to [60,61], Raman peaks were identified as: 1179–1182 cm^{-1}–sp^3-rich phase of the amorphous carbon; 1310–1314 cm^{-1}–*D* peak of microcrystalline highly disordered graphitic structure (that results from symmetry breaking at edges of graphite planes in sp^2 carbon material); 1503 cm^{-1}–vibrations of C—H in hydrogenated amorphous carbon or semicircle ring stretch vibration of condensed benzene rings; 1599 cm^{-1}–*G* peak of highly ordered sp^2 graphite (however, the origin of this peak might be also from olefinic chains in carbonaceous deposit [61]). The essential difference between deposits in both used catalysts are quantitative shares of amorphous sp^3-rich and highly disordered sp^2 graphitic phases − in the potassium-promoted catalyst a smaller (3.0% vs. 7.9%) relative amount of the sp3-rich phase of the amorphous carbon and a larger (67.1% vs. 58.6%) relative amount of graphitic phases is present.

The production of fibrous carbon deposits takes place through precipitation of dissolved carbon from metal crystallites [62]. In this process metal particles are usually lift towards the top by the grooving carbon deposits (Fig. S5) and [63,64].

Filamentous carbon deposits formed during the SRE reaction do not always deactivate catalysts because accessibility of the part of metal surface may remain not blocked and metal particles can still take a part in the reaction [51,62]. When nickel particles are pushed from the support surface by whiskers carbon, they are located at the ends of filaments and can be still accessible to reactants from the gas phase. In consequence, the course of the catalytic reaction may be changed. Nickel crystallites pushed by filamentous carbon are disconnected from the support and the Ni/CeO_2 or KNi/CeO_2 catalysts can begin to function as Ni/C, KNi/C, Ni/KC or KNi/KC catalysts. It was previously shown [3,6,53,55,65] that the selectivity of ethanol conversion reaction depends on the nature of the support used in the catalyst.

Montero et al. [50] showed that the catalyst deactivation is a complex process and suggested three-stage deactivation of the La_2O_3-αAl_2O_3-supported nickel catalyst by carbon deposits formed during SRE. In the first stage, a significant increase of filamentous carbon deposits occurred that during their growth lifted metal particles to tops of filaments and simultaneously decreased the metal particles size, without blocking of active sites and without significant deactivation of the active metal particles. The second stage is continuation of metal particles lifting by filamentous carbon and decreasing the size of metal

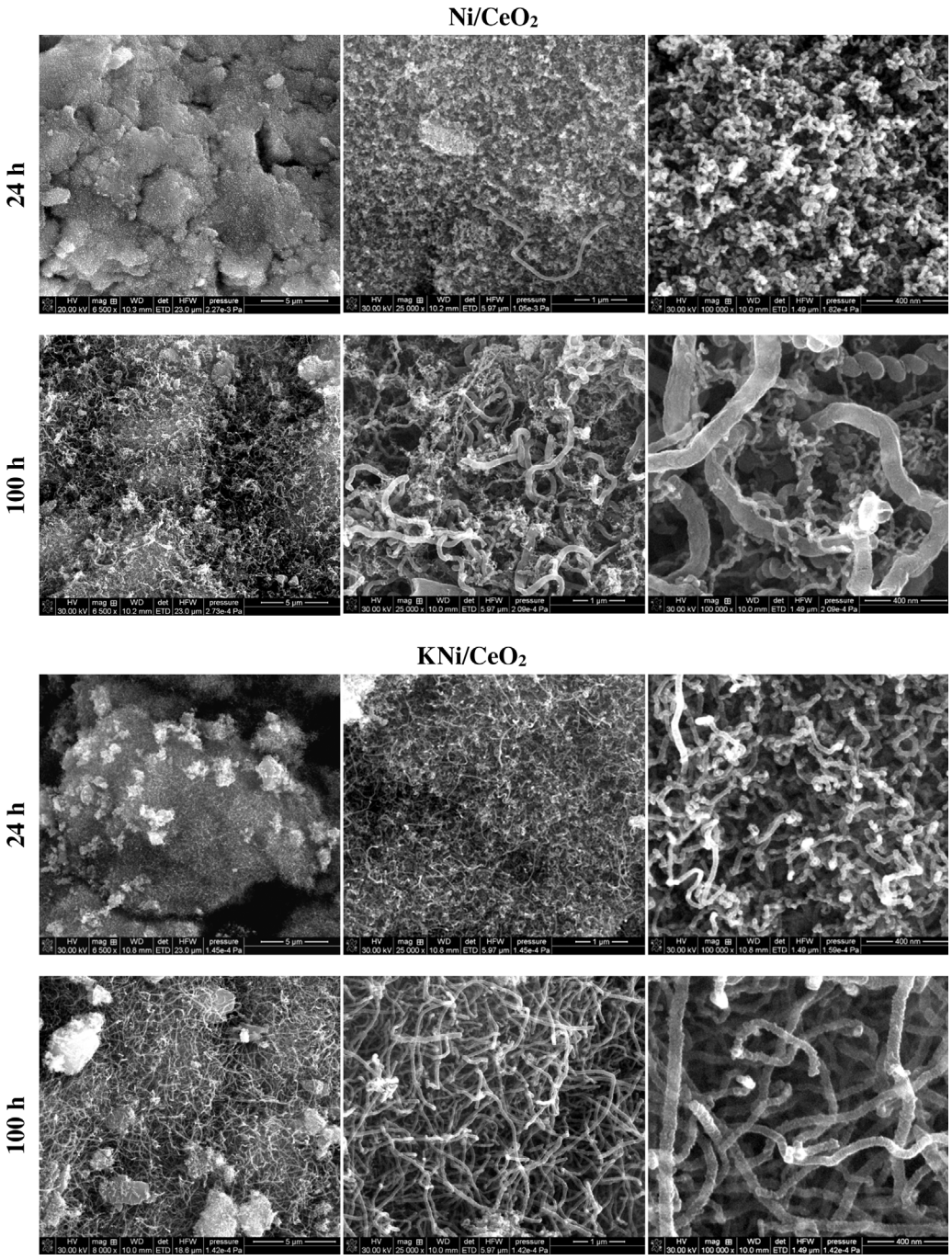

Fig. 22. SEM images of carbonaceous deposits in used Ni/CeO_2 and Ni/CeO_2 catalysts after 24 h and 100 h of the steam reforming of ethanol.

particles. Moreover, formation of filamentous carbon deposits is slowing down and its structure undergoes progressive condensation and graphitization. In this stage, the formation of non-filamentous (partially surrounding nickel crystallites) carbon deposits also increases. In the final stage, the ethanol conversion decreases because the catalyst is highly deactivated by carbon deposits. At this stage production of the carbon deposit is very slow and its dominant form is non-filamentous (partially surrounding) carbon with a structure which undergoes graphitization and causes gradually blocking of the active sites. These results show that the carbon deposits produced in the SRE are a combination of filamentous and non-filamentous carbon deposits which are formed by evolution of filamentous carbon [4,50].

Based on our results and results shown by Montero et al. [50] it can be suggested that the similar deactivation process occurs in the unpromoted and potassium-promoted ceria-supported nickel catalysts during the steam reforming of ethanol. Presented studies (Figs. 20, 21 and 24) showed that the carbon deposit formed on the nickel catalysts during the SRE reaction has amorphous and graphitic structures. Both structures are mixed with each other and they surround the crystallites of the nickel active phase only partially. Therefore, a part of the nickel active phase uncovered by carbon deposit can still participate in the SRE process.

Our microscopic and Raman results strongly suggest that faster deactivation of the potassium-promoted KNi/CeO_2 catalyst is caused by significant production (much larger than on the Ni/CeO_2 catalyst) of graphitic fibrous carbon deposit on its surface, which with time-on-stream can encapsulate a greater number of nickel active phase crystallites and causes them inactive in the SRE process. For formation of larger amounts of carbon deposits larger crystallites of the active phase are responsible [34]. Therefore, the KNi/CeO_2 catalyst, having larger

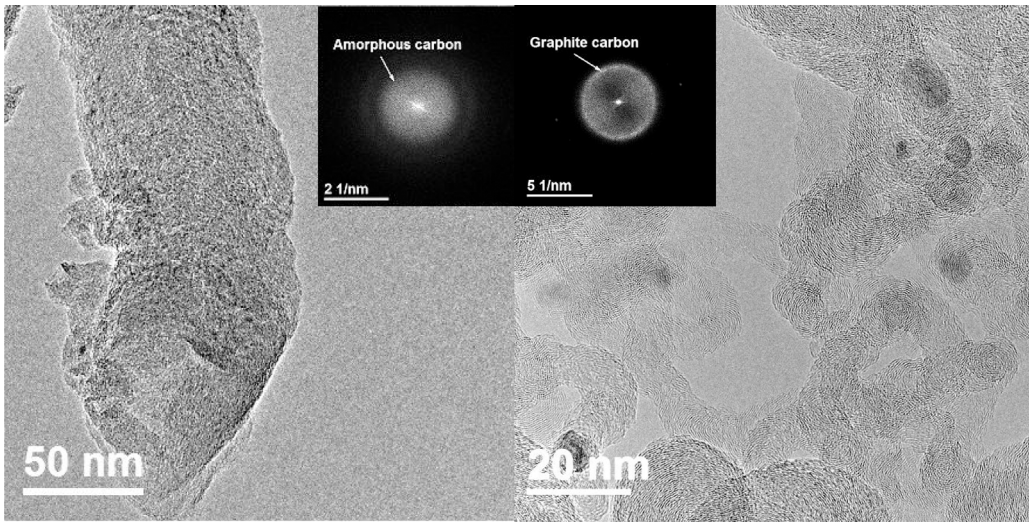

Fig. 23. HRTEM images of thick (amorphous – lack of graphite ring at FFT) and thick (graphitic – clear graphite ring at FFT) fibrous carbon deposits formed in the steam reforming of ethanol.

nickel crystallites than those in the Ni/CeO_2 catalyst, produces larger amounts of carbon deposits and undergoes faster deactivation in the SRE, even though potassium promoter was present. Formation of carbon deposits was facilitated by gradual agglomeration of potassium species on the catalyst surface during the SRE.

4. Conclusions

Presented results showed that both as-prepared ceria-supported nickel catalysts, unpromoted and potassium-promoted, contain nickel oxide crystallites of similar dimension. The activation (reduction) of the Ni/CeO_2 catalyst caused decreasing of the nickel crystallites size as compared to the initial nickel oxide crystallites, while potassium promoter increases nickel crystallites during reduction. Sintering of nickel crystallites is favoured by alkali. However, the addition of potassium promoter to the Ni/CeO_2 catalyst decreases the temperature necessary for activation of the nickel active phase. Crystallites of metallic nickel with the Fm3 m space group and the cubic crystal lattice were observed in both catalysts after reduction as well as after the reaction of the SRE, as the only form of the nickel active phase participating in the steam reforming of ethanol process. Under applied SRE conditions (420 °C, $EtOH/H_2O$ = 1/12 mol/mol) nickel crystallites in the unpromoted Ni/CeO_2 increased, while in the potassium-promoted KNi/CeO_2 their average size decreased, in comparison with those in the freshly reduced catalysts. It proves that in the latter catalyst original nickel crystallites underwent defragmentation by growing carbonaceous deposit. In both catalysts fragments of nickel active phase are pushed from the ceria support by carbon deposit formed during the reaction while the rest of nickel still remains on the ceria support surface.

Potassium promoter in the fresh (in the oxide form) KNi/CeO_2 catalyst is very good dispersed on the whole catalyst surface. The reduction does not change its distribution. However, under SRE reaction its dispersion changes − significant amount of potassium promoter is located on the ceria support while only much smaller amount of remaining promoter is located on the nickel active phase still deposited on the catalyst. Noticeable agglomeration of potassium species also appeared. Nickel which is pushed from the ceria support with carbonaceous deposit does not contain potassium.

The carbonaceous deposit of similar nature was formed under steam reforming of ethanol on both catalysts. The essential difference lies in the fact that on the potassium-promoted catalyst a smaller relative amount of the sp^3-rich phase of the amorphous carbon and a larger relative amount of graphitic phases is present. The potassium promoter in the KNi/CeO_2 catalyst does not protect it against formation of carbon deposit and does not improve its stability under applied SRE conditions. More important in this respect is a high dispersion of the nickel active phase. Our results showed that the crystallites size of the active phase has a much greater influence on amounts of the carbon deposit formed

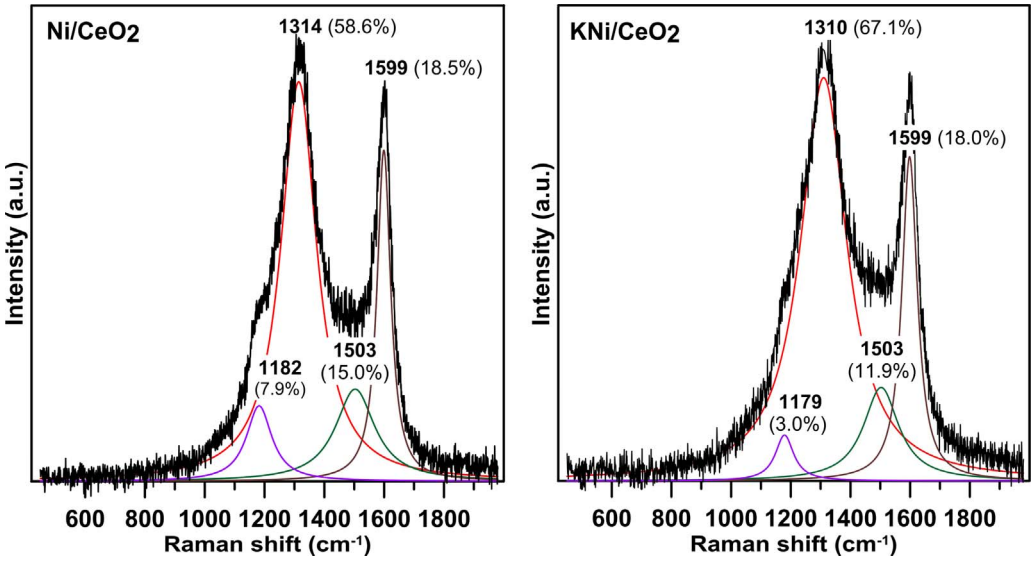

Fig. 24. Raman spectra and fitting results for carbonaceous deposits present in Ni/CeO_2 and KNi/CeO_2 catalysts used 100 h in the steam reforming of ethanol.

during the SRE reaction than the addition of the alkali promoter to the nickel catalyst. The larger crystallites of the active phase aid production of carbon deposit and accelerate deactivation of the catalyst in the SRE process, even if the potassium promoter is present in the catalyst. The unpromoted Ni/CeO_2 catalyst with smaller nickel crystallites than those in the potassium-promoted one shows better stability in the steam reforming of ethanol. It is supposed that smaller particles of the nickel active phase have a higher contribution of low-coordinated active centres, such as edges, corners and steps what increases stability, selectivity and activity of the catalyst in the SRE. Larger particles of the nickel active phase with higher contribution of active centres located on faces of crystallites we suggest as responsible for the lower stability, selectivity and activity of the catalyst and its faster deactivation.

On the Ni/CeO_2 catalyst two types of fibrous carbon deposits are formed in the SRE. The fibres of the first type are long and thick, with amorphous (disordered) structure. The carbonaceous fibres of the second type are short and thin of mostly graphitic structure. The KNi/CeO_2 catalyst, having larger nickel crystallites than those in the Ni/CeO_2 catalyst, produces in the SRE very large amounts of long and uniform medium-thick fibrous carbon deposit with mostly graphitic (ordered) structure. Their length and diameter are larger (already after 24 h of the SRE) than in the case of the unpromoted nickel catalyst. The formation of carbon deposits was facilitated by gradual agglomeration of potassium species on the catalyst surface during the SRE. Significant production (much intensive than on the Ni/CeO_2 catalyst) of graphitic fibrous carbon deposit on the surface of KNi/CeO_2 catalyst, which with time-of-stream can encapsulate and cause inactive a greater number of nickel active phase crystallites, is considered as responsible for faster deactivation of that catalyst in the SRE process.

Presented results showed also that direct measurements of the nickel crystallites size by the TEM allowed estimating that the optimum temperatures of hydrogen chemisorption for determination of the average size of nickel crystallites in the unpromoted and potassium-promoted ceria-supported nickel catalysts are 110 °C and 120 °C, respectively. Also, the higher temperatures, up to 140 °C, can be acceptable without significant errors in determination of the crystallites size. The average crystallites size in the unpromoted Ni/CeO_2 catalyst determined by the XRD method is different than that determined from TEM and hydrogen chemisorption data. The difference results from limitations of the standard XRD method which does not allow measuring small crystallites.

Acknowledgements

The research was carried out with the equipment purchased thanks to the financial support of the European Regional Development Fund in the framework of the Polish Innovation Economy Operational Program (contract no. POIG.02.01.00-06-024/09 Centre for Functional Nanomaterials; www.cnf.umcs.lublin.pl).

Appendix A. Supplementary data

Supplementary data associated with this article can be found, in the online version, at http://dx.doi.org/10.1016/j.apcatb.2017.09.052.

References

[1] V. Subramani, C. Song, Advances in catalysis and processes for hydrogen production from ethanol reforming, Catalysis 20 (2007) 65–106.
[2] P.R. de la Piscina, N. Homs, Use of biofuels to produce hydrogen (reformation processes), Chem. Soc. Rev. 37 (2008) 2459–2467.
[3] A. Haryanto, S. Fernando, N. Murali, S. Adhikari, Current status of hydrogen production techniques by steam reforming of ethanol: a review, Energy Fuel 19 (2005) 2098–2106.
[4] G. Słowik, M. Greluk, A. Machocki, Microscopic characterization of changes in the structure of KCo/CeO_2 catalyst used in the steam reforming of ethanol, Mater. Chem. Phys. 173 (2016) 219–237.
[5] W. Xu, Z. Liu, A.C. Johnston-Peck, S.D. Senanayake, G. Zhou, D. Stacchiola, E.A. Stach, J.A. Rodriguez, Steam reforming of ethanol on Ni/CeO_2: reaction pathway and interaction between Ni and the CeO_2 support, ACS Catal. 3 (2013) 975–984.
[6] L.V. Mattos, G. Jacobs, B.H. Davis, F.B. Noronha, Production of hydrogen from ethanol: review of reaction mechanism and catalyst deactivation, Chem. Rev. 112 (2012) 4094–4123.
[7] G.Y. Ramírez-Hernández, T. Viveros-García, R. Fuentes-Ramírez, I.R. Galindo-Esquivel, Promoting behavior of yttrium over nickel supported on alumina-yttria catalysts in the ethanol steam reforming reaction, Int. J. Hydrogen Energ. 41 (2016) 9332–9343.
[8] H.V. Fajardo, L.F.D. Probst, N.L.V. Carreño, I.T.S. Garcia, A. Valentini, Hydrogen production from ethanol steam reforming over Ni/CeO_2 nanocomposite catalysts, Catal. Lett. 119 (2007) 228–236.
[9] Ch. Zhang, S. Li, G. Wu, J. Gong, Synthesis of stable $Ni-CeO_2$ catalysts via ball-milling for ethanol steam reforming, Catal. Today 233 (2014) 53–60.
[10] A. Kubacka, M. Fernández-García, A. Martínez-Arias, Catalytic hydrogen production through WGS or steam reforming of alcohols over Cu, Ni and Co catalysts, Appl. Catal. A 518 (2016) 2–17.
[11] J. Lorca, N. Homs, P.R. de la Piscina, In situ DRIFT-mass spectrometry study of the ethanol steam-reforming reaction over carbonyl-derived Co/ZnO catalysts, J. Catal 227 (2004) 556–560.
[12] J. Xu, X. Zang, R. Zenobi, J. Yoshinobu, Z. Xu, J.T. Yates, Ethanol decomposition on Ni (111): observation of ethoxy formation by IRAS and other methods, Surf. Sci. 256 (1991) 288–300.
[13] B. Zhang, X. Tang, Y. Li, W. Cai, Y. Xu, W. Shen, Steam reforming of bio-ethanol for the production of hydrogen over ceria-supported Co, Ir and Ni catalysts, Catal. Commun. 7 (2006) 367–372.
[14] J. Carrasco, L. Barrio, P. Liu, J.A. Rodriguez, M.V. Ganduglia-Pirovano, Theoretical studies of the adsorption of CO and C on Ni (111) and Ni/CeO_2 (111): evidence of a strong metal–support interaction, J. Phys. Chem. C 117 (2013) 8241–8250.
[15] F. Frusteri, S. Freni, V. Chiodo, L. Spadaro, O. Di Blasi, G. Bonura, S. Cavallaro, Steam reforming of bio-ethanol on alkali-doped Ni/MgO catalysts: hydrogen production for MC fuel cell, Appl. Catal. A 270 (2004) 1–7.
[16] P. Rybak, B. Tomaszewska, A. Machocki, W. Grzegorczyk, A. Denis, Conversion of ethanol over supported cobalt oxide catalysts, Catal. Today 176 (2011) 14–20.
[17] N. Laosiripojana, S. Assabumrungrat, Catalytic dry reforming of methane over high surface area ceria, Appl. Catal. B 60 (2005) 107–116.
[18] N. Laosiripojana, S. Assabumrungrat, Synthesis gas production from dry reforming of methane over CeO_2 doped Ni/Al_2O_3: influence of the doping ceria on the resistance toward carbon formation, Appl. Catal. B 66 (1–2) (2006) 29–39.
[19] H. Song, B. Tan, U.S. Ozkan, Novel synthesis techniques for preparation of Co/CeO_2 as ethanol steam reforming catalysts, Catal. Lett. 132 (2009) 422–429.
[20] H. Song, B. Mirkelamoglu, U.S. Ozkan, Effect of cobalt precursor on the performance of ceria-supported cobalt catalysts for ethanol steam reforming, Appl. Catal. A 382 (2010) 58–64.
[21] G. Słowik, A. Gawryszuk-Rżysko, M. Greluk, A. Machocki, Estimation of average crystallites size of active phase in ceria-supported cobalt-based catalysts by hydrogen chemisorption vs TEM and XRD methods, Catal. Lett. 146 (10) (2016) 2173–2184.
[22] A. Borodziński, M. Bonarowska, Relation between crystallite size and dispersion on supported metal catalysts, Langmuir 13 (1997) 5613–5620.
[23] J.L. Carter, J.A. Cusumano, J.H. Sinfelt, Catalysis over supported metals. V. The effect of crystallite size on the catalytic activity of nickel, J. Phys. Chem. 70 (1966) 2257–2263.
[24] L. Kępiński, Transmission Electron Microscopy as indispensable tool for imaging and chemical characterization of heterogeneous catalysts, Ann. Univ. M. Curie-Sklodowska (2010) 9–19 LXV, 2, Sect. AA.
[25] G.A. Tritsaris, J. Greeley, J. Rossmeisl, J.K. Nørskov, Atomic-scale modeling of particle size effects for the oxygen reduction reaction on Pt, Catal. Lett. 141 (2011) 909–913.
[26] J. Greeley, J. Rossmeisl, J. Hellman, J. Nørskov, Theoretical trends in particle size effects for the oxygen reduction reaction, Z. Phys. Chem. 221 (2007) 1209–1220.
[27] Y. Yuan, N. Yan, P.J. Dyson, Advances in the rational design of rhodium nanoparticle catalysts: control via manipulation of the nanoparticle core and stabilizer, ACS Catal. 2 (2012) 1057–1069.
[28] M.A. Aramendia, V. Borau, C. Jiménez, J.M. Marinas, A. Moreno, Comparative measurements of the dispersion of Pd catalyst on SiO_2 $AlPO_4$ support using TEM and H_2 chemisorption, Colloids Surf. A 106 (1996) 161–165.
[29] J. Xiong, Ø. Borg, E.A. Blekkan, A. Holmen, Hydrogen chemisorption on rhenium-promoted γ-alumina supported cobalt catalysts, Catal. Commun. 9 (2008) 2327–2330.
[30] J.M. Zowtiak, G.D. Weatherbee, C.H. Bartholomew, Activated adsorption of H_2 on cobalt and effects of support thereon, J. Catal. 82 (1983) 230–235.
[31] J.M. Zowtiak, C.H. Bartholomew, The kinetics of H_2 adsorption on and desorption from cobalt and the effects of support thereon, J. Catal. 83 (1983) 107–120.
[32] R.C. Reuel, C.H. Bartholomew, The stoichiometries of H_2 and CO adsorptions on cobalt: effects of support and preparation, J. Catal. 85 (1984) 63–77.
[33] S.H. Ogo, T. Shimizu, Y. Nakazawa, K. Mukawa, D. Mukai, Y. Sekine, Steam reforming of ethanol over K promoted Co catalyst, Appl. Catal. A 495 (2015) 30–38.
[34] D. Zanchet, J.B.O. Santos, S. Damyanova, J.M.R. Gallo, J.M.C. Bueno, Toward understanding metal-catalyzed ethanol reforming, ACS Catal. 5 (2015) 3841–3863.
[35] A. Navrotsky, C. Ma, K. Lilova, N. Birkner, Nanophase transition metal oxides show large thermodynamically driven shifts in oxidation-reduction equilibria, Science 330 (2010) 199–201.
[36] R. van Hardeveld, F. Hartog, Influence of metal particle size in nickel-on-aerosil catalysts on surface site distribution catalytic activity, and selectivity, Adv. Catal.

22 (1972) 75–113.
[37] R.U. Ribeiro, J.W.C. Liberatori, H. Winnishofer, J.M.C. Bueno, D. Zanchet, Colloidal Co nanoparticles supported on SiO_2: Synthesis, characterization and catalytic properties for steam reforming of ethanol, Appl. Catal. B 91 (2009) 670–678.
[38] A.L.M. da Silva, J.P. den Breejen, L.V. Mattos, J.H. Bitter, K.P. de Jong, F.B. Noronha, Cobalt particle size effects on catalytic performance for ethanol steam reforming–smaller is better, J. Catal. 318 (2014) 67–74.
[39] R.C. Reuel, C.H. Bartholomew, Effects of support and dispersion on the CO hydrogenation activity/selectivity properties of cobalt, J. Catal. 85 (1984) 78–88.
[40] A.M. Hilmen, D. Schanke, K.F. Hanssen, A. Holmen, Study of the effect of water on alumina supported cobalt Fischer–Tropsch catalysts, Appl. Catal. A 186 (1999) 169–188.
[41] X. Du, D. Zhang, L. Shi, R. Gao, J. Zhang, Morphology dependence of catalytic properties of Ni/CeO_2 nanostructures for carbon dioxide reforming of methane, J. Phys. Chem. C 116 (2012) 10009–10016.
[42] Z. Gao, Q. Dai, H. Ma, Z. Li, Ceria supported nickel catalysts for CO removal from H_2-rich gas, J. Rare Earth. 34 (2016) 1213–1220.
[43] J.-Y. Luo, M. Meng, X. Li, X.-G. Li, Y.-Q. Zha, T.-D. Hu, Y.-N. Xie, J. Zhang, Mesoporous Co_3O_4–CeO_2 and Pd/Co_3O_4–CeO_2 catalysts: synthesis, characterization and mechanistic study of their catalytic properties for low-temperature CO oxidation, J. Catal. 254 (2008) 310–324.
[44] F. Giordano, A. Trovarelli, C. de Leitenburg, M. Giona, A model for the temperature-programmed reduction of low and high surface area ceria, J. Catal. 193 (2000) 273–282.
[45] J. El Fallah, S. Boujana, H. Dexpert, A. Kiennemann, J. Majerus, O. Touret, F. Villain, F. Le Normand, Redox processes on pure ceria and on Rh/CeO_2 catalyst monitored by X-ray absorption (Fast Acquisition Mode), J. Phys. Chem. 98 (1994) 5522–5533.
[46] S. Tada, T. Shimizu, H. Kameyama, T. Heneda, R. Kikuchi, Int. J. Hydrogen Energy 37 (2012) 5527–5531.
[47] P.D. Vaidya, A.E. Rodrigues, Insight into steam reforming of ethanol to produce hydrogen for fuel cells, Chem. Eng. J. 117 (2006) 39–49.
[48] S.M. de Lima, R.C. Colman, G. Jacobs, B.H. Davis, K.R. Souza, A.F.F. de Lima, L.G. Appel, L.V. Mattos, F.B. Noronha, Ni/CeO_2 catalysts with high CO_2 methanation activity and high CH_4 selectivity at low temperatures, Catal. Today 146 (2009) 110–123.
[49] R.M. Navarro, M.A. Peña, J.L.G. Fierro, Hydrogen production reactions from carbon feedstocks: fossil fuels and biomass, Chem. Rev. 107 (2007) 3952–3991.
[50] C. Montero, A. Ochoa, P. Castaño, J. Bilbao, A.G. Gayubo, Monitoring Ni^0 and coke evolution during the deactivation of a Ni/La_2O_3–αAl_2O_3 catalyst in ethanol steam reforming in a fluidized bed, J. Catal. 331 (2015) 181–192.
[51] J. Vicente, J. Ereña, C. Montero, M.J. Azkoiti, J. Bilbao, A.G. Gayubo, Reaction pathway for ethanol steam reforming on a Ni/SiO_2 catalyst including coke formation, Int. J. Hydrogen Energy 39 (2014) 18820–18834.
[52] F. Mariño, M. Boveri, G. Baronetti, M. Laborde, Hydrogen production via catalytic gasification of ethanol. A mechanism proposal over copper–nickel catalysts, Int. J. Hydrogen Energy 29 (2004) 67–71.
[53] J. Vicente, C. Montero, J. Ereña, M.J. Azkoiti, J. Bilbao, A.G. Gayubo, Coke deactivation of Ni and Co catalysts in ethanol steam reforming at mild temperatures in a fluidized bed reactor, Int. J. Hydrogen Energy 39 (2014) 12586–12596.
[54] V.D. Santo, A. Gallo, A. Naldoni, M. Guidotti, R. Psaro, Bimetallic heterogeneous catalysts for hydrogen production, Catal. Today 197 (2012) 190–205.
[55] R. Trane-Restrup, S. Dahl, A.D. Jensen, Steam reforming of ethanol: effects of support and additives on Ni-based catalysts, Int. J. Hydrogen Energy 38 (2013) 15105–15118.
[56] H.S.J.K. Bengaard. Nørskov, J.B.S. Sehested. Clausen, L.P. Nielsen, A.M. Molenbroek, J.R. Rostrup-Nielsen, Steam reforming and graphite formation on Ni catalysts, J. Catal. 209 (2002) 365–384.
[57] S.J. Murray, D.A. Brooks, F.M. Leibsle, R.D. Diehl, R. McGrath, Oxygen-induced ordering of potassium in a coadsorbate phase: a SPA-LEED and STM study of K-O/Ni (l00), Surf. Sci. 314 (1994) 307–314.
[58] P. Finetti, G.S. Leatherman, M. Caragiu, M. Lindroos, R.R.D. McGrath. Diehl, Low-energy electron diffraction study of the surface geometry of $Ni(100)-(3 \times 3)$-K + 4O, Surf. Sci. 462 (2000) 77–84.
[59] S. Turczyniak, M. Greluk, G. Słowik, W. Gac, S. Zafeiratos, A. Machocki, Surface state and catalytic performance of ceria-supported cobalt catalysts in the steam reforming of ethanol, ChemCatChem 9 (2017) 782–797.
[60] Y. Wang, D.C. Alsmeyer, R.L. McCreery, Raman spectroscopy of carbon materials: structural basis of observed spectra, Chem. Mater. 2 (1990) 557–563.
[61] J. Schwan, S. Ulrich, V. Batori, H. Ehrhardt, S.R.P. Silva, Raman spectroscopy on amorphous carbon films, J. Appl. Phys. 80 (1996) 440–447.
[62] J.R. Rostrup-Nielsen, Catalytic steam reforming, in: J.R. Anderson, M. Boudart (Eds.), Catalysis: Science and Technology V, Springer, 1984, pp. 73–93.
[63] C.H. Bartholomew, Carbon deposition in steam reforming and methanation, Catal. Rev. Sci. Eng. 24 (1) (1982) 67–112.
[64] S.M. de Lima, A.M. da Silva, L.O.O. da Costa, U.M. Graham, G. Jacobs, B.H. Davis, L.V. Mattos, F.B. Noronha, Study of catalyst deactivation and reaction mechanism of steam reforming, partial oxidation, and oxidative steam reforming of ethanol over Co/CeO_2 catalyst, J. Catal. 268 (2009) 268–281.
[65] A.N. Fatsikostas, X.E. Verykios, Reaction network of steam reforming of ethanol over Ni-based catalysts, J. Catal. 225 (2004) 439–452.